Fl 12

ADA031577

DNA 3967Z

DATA REDUCTION AND ANALYSIS- EXPERIMENTAL IEMP/SGEMP ELECTRON BEAM STUDY, FIRST INTERM REPORT: 40 KEV BEAM ENERGY

Kaman Sciences Corporation
P.O. Box 7463
Colorado Springs, Colorado 80933

December 1975

Interim Report

CONTRACT No. DNA 001-75-C-0167

THIS WORK SPONSORED BY THE DEFENSE NUCLEAR AGENCY
UNDER RDT&E RMSS CODE B323075464 R99QAXEB08953 H2590D.

Prepared for
Director
DEFENSE NUCLEAR AGENCY
Washington, D. C. 20305

Destroy this report when it is no longer needed. Do not return to sender.

UNCLASSIFIED

SECURITY CLASSIFICATION OF THIS PAGE (When Data Entered)

19 REPORT DOCUMENTATION PAGE

READ INSTRUCTIONS BEFORE COMPLETING FORM

1. REPORT NUMBER 18 DNA 3967Z	2. GOVT ACCESSION NO.	3. RECIPIENT'S CATALOG NUMBER
4. TITLE (and Subtitle) 6 DATA REDUCTION AND ANALYSIS-EXPERIMENTAL IEMP/SGEMP ELECTRON BEAM STUDY, FIRST INTERIM REPORT: 40 KEV BEAM ENERGY		5. TYPE OF REPORT & PERIOD COVERED ~~Interim~~ Report 6. PERFORMING ORG. REPORT NUMBER 14 K-75-107U(R)
7. AUTHOR(s) 10 R. J. Fisher R. L. Hartman		8. CONTRACT OR GRANT NUMBER(s) 15 DNA 001-75-C-0167 NEW
9. PERFORMING ORGANIZATION NAME AND ADDRESS Kaman Sciences Corporation P.O. Box 7463 Colorado Springs, Colorado 80933		10. PROGRAM ELEMENT, PROJECT, TASK AREA & WORK UNIT NUMBERS ~~Subtask~~ R99QAXEB089-53
11. CONTROLLING OFFICE NAME AND ADDRESS Director Defense Nuclear Agency Washington, D.C. 20305		12. REPORT DATE 11 Dec[redacted] [redacted]75 13. NUMBER OF PAGES 60
14. MONITORING AGENCY NAME & ADDRESS (if different from Controlling Office) 12 51p.		15. SECURITY CLASS (of this report) UNCLASSIFIED 15a. DECLASSIFICATION/DOWNGRADING SCHEDULE

16. DISTRIBUTION STATEMENT (of this Report)

Approved for public release; distribution unlimited.

17. DISTRIBUTION STATEMENT (of the abstract entered in Block 20, if different from Report)

18. SUPPLEMENTARY NOTES

This work sponsored by the Defense Nuclear Agency under RDT&E RMSS Code B323075464 R99QAXEB08953 H2590D.

19. KEY WORDS (Continue on reverse side if necessary and identify by block number)

SGEMP Simulation
Electron Beam Experiments
IEMP Simulation
Electromagnetic Pulse (EMP)

20. ABSTRACT (Continue on reverse side if necessary and identify by block number)

This report ~~is~~ Kaman Sciences' first formal interim report which presents reduced data from the series of internal electromagnetic pulse (IEMP) simulation experiments was carried out by the Ballistic Missile Defense System Command, ~~early in 1974~~ and it also presents reduced time history and tabular data on selected pressures for the nominal 40 keV mean-energy injected beam.

DD FORM 1473 1 JAN 73 EDITION OF 1 NOV 65 IS OBSOLETE

UNCLASSIFIED

SECURITY CLASSIFICATION OF THIS PAGE (When Data Entered)

389119

20. ABSTRACT (Continued)

Details of the experimental apparatus and techniques are found in the following reference: "A Study of IEMP/SGEMP Phenomenology Using Electron Beam Simulation;" also, additional discussion is presented in Appendix B in this report. Additional similar interim reports will cover the remaining two sets of data comprising the nominal 60 keV mean-energy beam into the 18 cm length chamber and nominal 125 keV beam into the 30 cm length chamber.

A final report will contain analyses and correlation of the three data sets covered in the interim reports as well as the 60 keV data set previously reduced and reported on in the above-mentioned reference. The final report will also contain results of computer calculations using Kaman Sciences' two-dimensional code EBBTIDE for comparison with appropriate determined quantities.

PREFACE

The bulk of the data processing techniques and codes employed in reducing the data presented in this report were developed under the leadership of Dr. J. S. Duval prior to his leaving Kaman Sciences to join the U. S. Geological Survey. Additional discussions with him during the course of the work presented herein are also acknowledged with pleasure.

TABLE OF CONTENTS

ILLUSTRATIONS

ILLUSTRATIONS (Cont'd)

ILLUSTRATIONS (Cont'd)

DATA REDUCTION AND ANALYSIS-
EXPERIMENTAL IEMP/SGEMP ELECTRON BEAM STUDY,
FIRST INTERIM REPORT: 40 keV BEAM ENERGY

I. INTRODUCTION

The following report is Kaman Sciences' first formal interim report to the Defense Nuclear Agency on work supported under contract number DNA001-75-C-0167. Presented herein are reduced data from the series of internal electromagnetic pulse (IEMP) simulation experiments carried out under sponsorship of the Ballistic Missile Defense System Command, contract number DASG60-74-C-0015, early in 1974.

The experiments carried out were designed to explore under controlled laboratory conditions the phenomenology governing the behavior of a uniformly distributed beam of electrons injected axially into a test chamber of cylindrical geometry and to provide a reliable body of experimental data against which to evaluate existing or evolving system generated electromagnetic pulse (SGEMP) computational codes.

The cylindrical experimental chamber was instrumented in such a manner as to provide correlated time history data on transmitted currents as a function of radial location and wall currents, radial current densities and magnetic fields as a function of axial location. Additionally, radial electric field measurements were attempted using short monopole stubs, but plasma sheathing complications rendered those data unusable.

A 30 cm diameter monoenergetic electron beam generated using the Simulation Physics Incorporated SPI 5000 machine was injected axially into the experimental chamber through an aluminized mylar membrane. Suitably gasketed to complete the vacuum tight integrity of the chamber, this transmitting anode of the machine diode formed the entrance plate and allowed the drift chamber to be maintained at a fixed pressure for each shot. The pressure range explored extended from less than one micron to, in some instances, twenty torr. The time histories of the quantities enumerated above along with electron beam machine diagnostic voltage and current outputs were monitored for each shot on twenty-three separate data channels (each equalized to 350 MHz bandwidth) and displayed on Tektronix 519 oscilloscopes. The total body of data acquired corresponded to three different mean energies of the injected beam - 40, 60, and 125 keV; two different chamber lengths, 18 and 30 cm; and the pressure range stated above.

Details of the experimental apparatus and techniques are to be found in reference (1). Additional discussion is also presented in Appendix B of this report. This report will present reduced time history and tabular data on selected pressures for the nominal 40 keV mean-energy injected beam. The length of the test chamber was 30 cm and the injected current pulse length was 30 nsec FWHM. Additional similar interim reports will cover the remaining two sets of data comprising the nominal 60 keV mean-energy beam into the 18 cm length chamber and nominal 125 keV beam into the 30 cm length chamber. A final report will contain analyses and correlations of the three data sets covered in the interim reports as well as the 60 keV data set previously reduced and reported on in reference (1). The final report will also contain results of

computer calculations using Kaman Sciences' two-dimensional code EBBTIDE for comparison wtih appropriate experimentally determined quantities. EBBTIDE provides a self-consistent, fully electromagnetic solution to charged particle electrodynamic problems. Comparisons of EBBTIDE calculations to date have been against electron beam experimental data corresponding to end-on photon illumination of a right circular cylinder and against underground test data of a right circular cylinder enclosing a sphere located on the axis of the cylinder. Results from the three-dimensional code TRIFIC, which uses the same basic algorithms as EBBTIDE, have also been compared against underground test data corresponding to side-on illumination of concentric right circular cylinders. In all cases, agreement has been to within a factor of two in amplitude and waveshape.

The remainder of this report has been organized into four main sections contained in Sections II, III, IV and V. Section II describes the process which has been used to obtain the characterization of the injected electron beam mean energy and current (as a function of time). Section II contains time history waveforms of various data categories. Section IV contains summary tables and plots of selected data from Section III. Finally, Section V discusses the experimental and processing errors inherent in the data of Section III.

II. CHARACTERIZATION OF THE INJECTED ELECTRON BEAM

A reliable working understanding of the nature of the injected beam is of course crucial in interpreting and applying the experimental results to actual systems situations. Additionally, an accurate specification of the injected beam in terms of energy, current density and angular distribution is required input to any computer code which is intended to simulate IEMP phenomena occurring within the chamber. A detailed comp. :ison of experimental vs computed results using

Kaman's EBBTIDE code is to be presented in the final report on this project. The curves presented in this section will serve to characterize the injected beam in sufficient detail to allow useful interpretation of the experimental results presented within the report.

As is discussed in reference (1)*, the injected 60 keV electron beam used in generating the data presented therein can be considered quite uniform over its entire diameter. Recent evidence, however, has appeared indicating that under the operating conditions of the SPI PULSE 5000 electron beam machine used to generate shorter pulse, lower energy data such as that presented herein, the injected beam may assume a degree of nonuniformity. This nonuniformity is manifested in a current density distribution in which the beam center is less dense than the beam edge by something on the order of a factor of one half. This circumstance is of critical importance in the context of code comparison against the experimental data and will have to be considered when defining the code input.

Three additional quantities beyond uniformity must be specified in order to fully characterize the injected beam which drives the experiment; beam energy, current density and angular distribution of the injected electrons. Appendix III of reference (1) discusses in detail the considerations and procedures involved in converting the machine diagnostic outputs corresponding to shank voltage and total diode current to the more pertinent quantities of interest, namely, injected beam energy and current density. Briefly, what is required is to correct the machine voltage monitor output for the inductive voltage drop between the monitor itself and the diode gap in

---
* Reference (1). Duval, J.S., Rich, W.F., and Clarke, C.A. "A Study of IEMP/SGEMP Phenomenology Using Electron Beam Simulation." Kaman Sciences Report (K-74-126U(R), November, 1974.

which the electron beam is generated. With the correction applied, the resultant voltage waveform represents the time history of the accelerating potential applied to the electrons emitted from the diode cathode. At each instant in time, the electrons impinging upon the anode plane have an essentially monoenergetic distribution which corresponds to the potential difference that has accelerated them across the diode gap. In order to arrive finally at the energy distribution of the injected beam, the impinging electron beam must be transported through the .25 mil aluminized mylar diaphram and wire mesh which constitutes the diode gap anode. Reference (1) contains curves generated by the Monte Carlo code EPIC which, when applied to the indicent electron beam, yield mean energy, angular distribution and current density of the beam which is ultimately injected into the test chamber.

Figure 1 presents the "typical" machine voltage monitor waveform associated with the group of data presented in this report. This waveform was constructed by computing the mean and standard deviation values of the individual machine voltage waveforms (calibration factor of 9.8 kv/v) at two nanosecond intervals for each shot in the series included in this report. The center curve represents the mean or the "typical" waveform, while the upper and lower curves represent the $\pm\sigma$ values.

The inductive voltage correction described above depends upon an $L\frac{dI}{dt}$ term in which I is the current flowing in the diode circuit, namely the current measured on the machine current monitor (calibration factor of 64 amp/volt). A "typical" machine current waveform was generated in the same manner as described above for machine voltage. Figure 2 presents the resulting curves. The mean curve shown in this figure was implemented in correcting the machine voltage in Figure 1. The curve in Figure 3 represents the resulting diode-gap or electron-accelerating voltage.

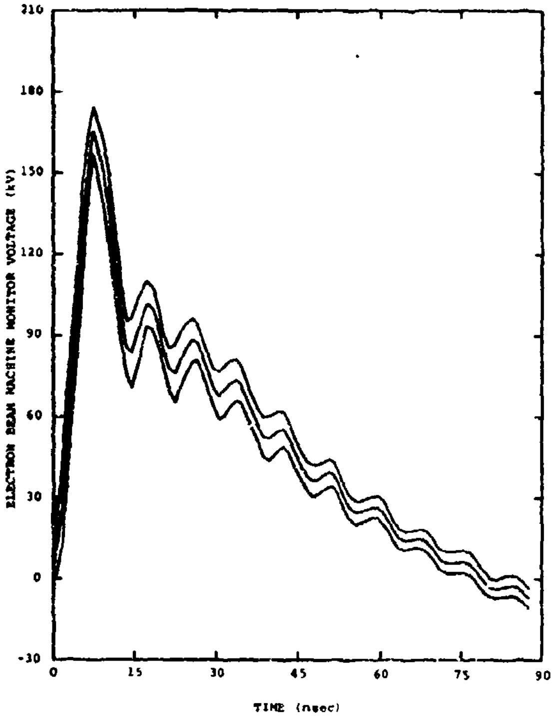

Figure 1. "Typical" machine voltage monitor output. Center curve is the mean of 14 shots; upper and lower curves are standard deviations.

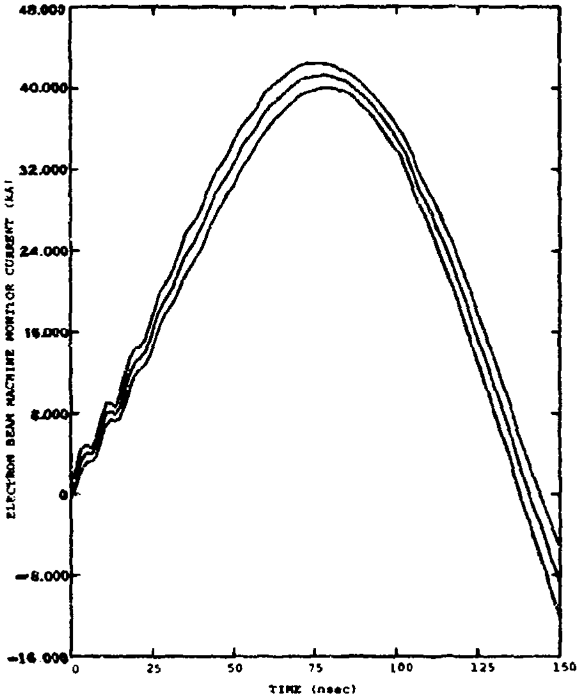

Figure 2. "Typical" machine current monitor output.

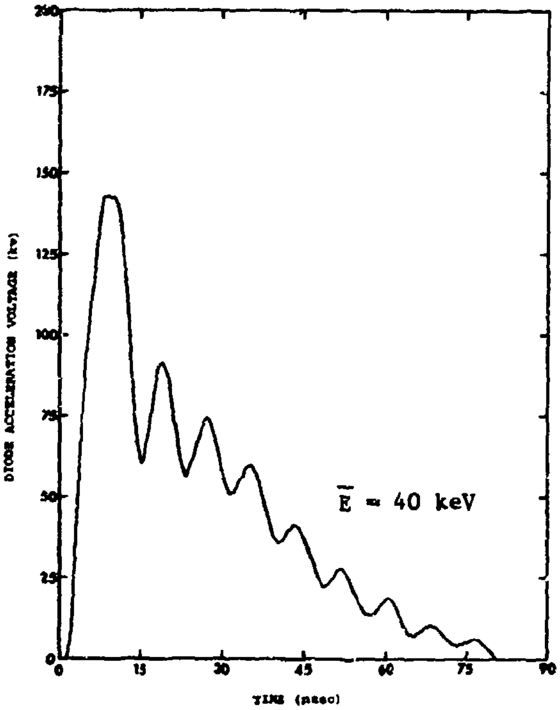

Figure 3. Electron beam machine diode gap accelerating voltage.

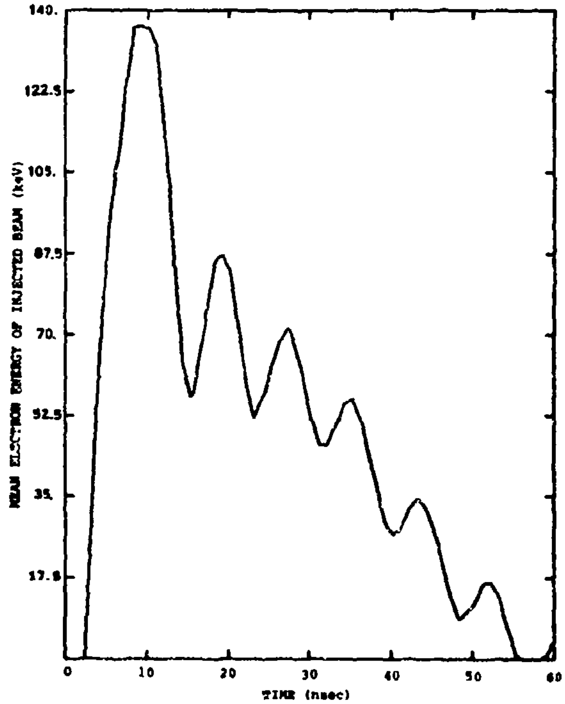

Figure 4. Injected beam electron mean energy corresponding to the machine voltage in Figure 1.

Figure 4 presents mean injected-beam energy vs time corresponding to the "typical" waveform in Figure 1. This figure can be used to determine the mean energy of the injected beam corresponding to the machine voltage output in Figure 1 for any instant in time.

The second beam quantity of interest is current density. Figure 5 displays the injected beam current measured on a solid aluminum plate 1 cm behind the machine anode plane. (A discussion of the errors in the injected current measurement is to be found on page 172 of reference (1). Recently available data on the injected current suggests that, due to space charge limiting very close to the injection plane, Figure 5 may be in error on the low side.)

III. PRESENTATION OF DATA

Data acquired using the 40 keV beam described in the previous section included time-correlated and dependent moebius-loop $\dot{B}$ data, total and spatially-resolved transmitted currents, collected wall currents and localized radial current density. In this section are presented time history curves of data from each of these categories. It should be noted that during processing, the polarities of some of the sets of time history data presented in this section have been inverted. This is, of course, incidental and, once noted, should not cause difficulty in interpretation of the data.

Magnetic Fields

Because of the relatively low signal-to-noise ratio inherent in the 40 keV data considerable difficulty was encountered in the processing of the $\dot{B}$ loop outputs in this data group. In particular, the integration process required in converting the moebius loop output to magnetic fields is quite sensitive to systematic digitizing errors

resulting from imprecision in establishing the zero reference as discussed in Section V. This is of course true for all cases, but the problem is compounded from a relative error point of view when the signal amplitudes are small as in this instance. This difficulty is discussed in Section V.

Figures 6a through 6j display magnetic fields obtained over the pressure range of 5 to 800 microns. In these and subsequent figures, the individual curves are displaced vertically simply as a convenience for presentation purposes so that the progression of behavior as a function of pressure is apparent.

Transmitted Current

The curves in Figures 7a and 7b display the total transmitted currents collected on the solid chamber endplate as a function of time and cavity pressure.

Figures 8a through 8m display the currents detected on each of the individual concentric rings which constitute the chamber endplate. These rings permit resolution of the radial distribution of the transmitted current into five regions. However, the rings can be driven in an antenna mode at times in the presence of high frequency radial electric fields. (See reference (1), p. 183.) Hence in some cases they do not respond as simple current collectors and thus some care is indicated in the interpretation of their output. Table I gives the dimensions of the endplate collection rings, which are approximately equal in area.

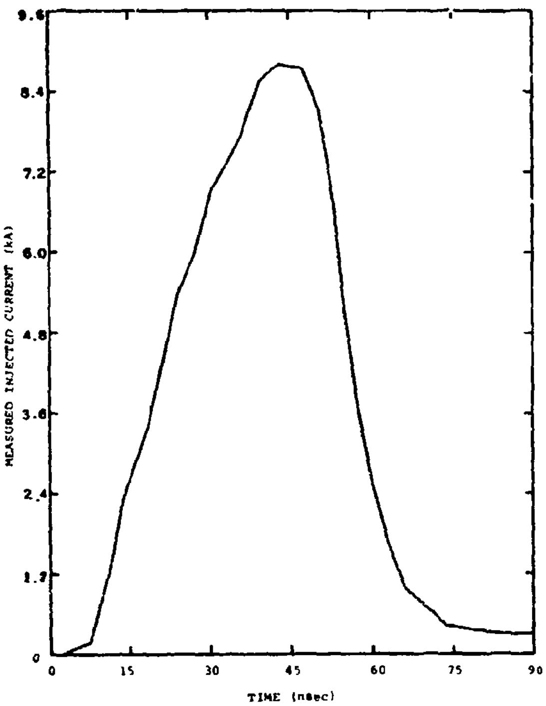

Figure 5. Measured injected current.

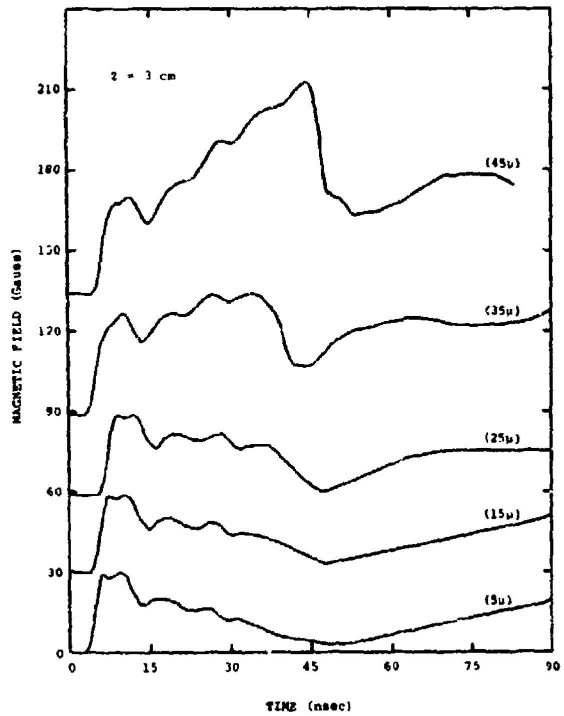

Figure 6a. Magnetic fields at Z=3 cm near chamber wall.

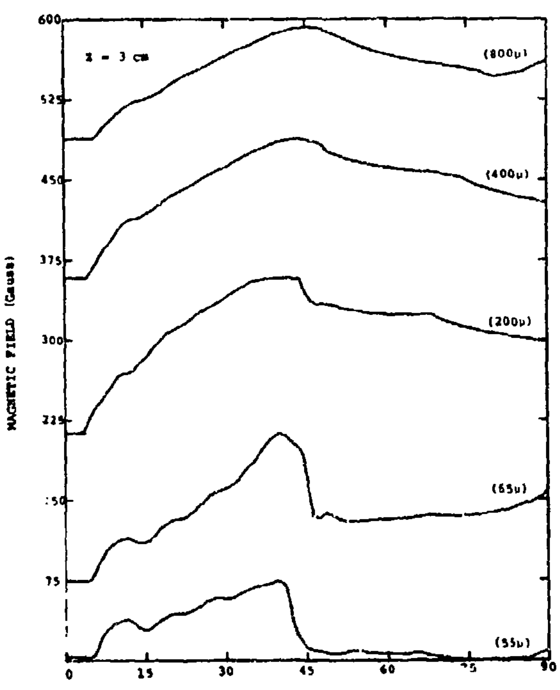

Figure 6b. Magnetic fields at Z=3 cm near chamber wall.

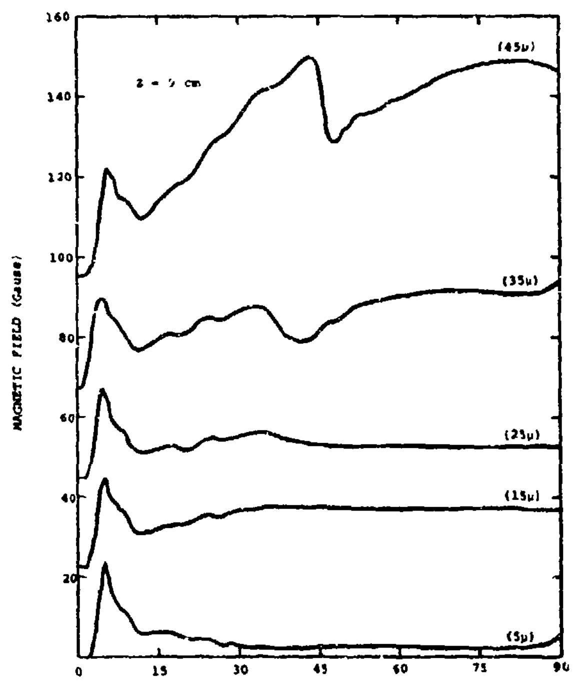

Figure 6c. Magnetic fields at Z=9 cm near chamber wall.

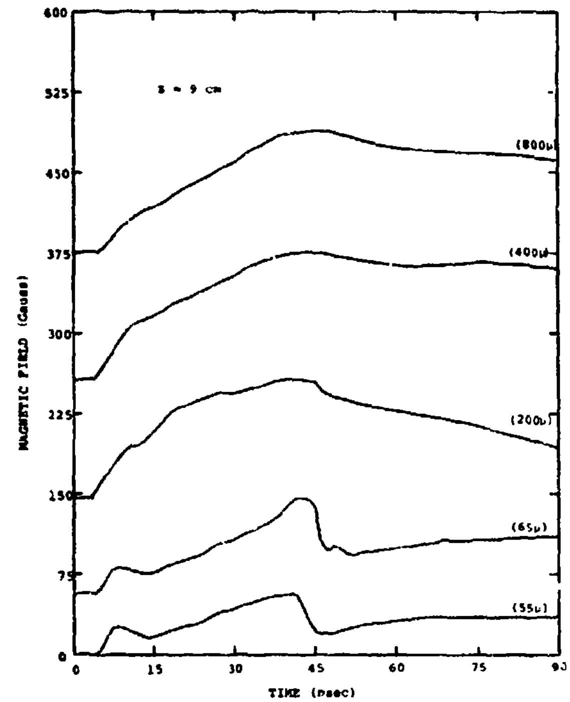

Figure 6d. Magnetic fields at Z=9 cm near chamber wall.

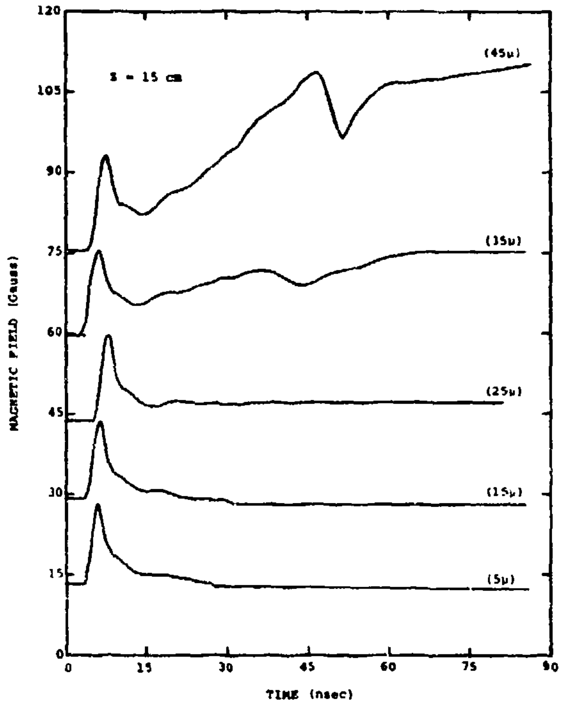

Figure 6e. Magnetic fields at Z=15 cm near chamber wall.

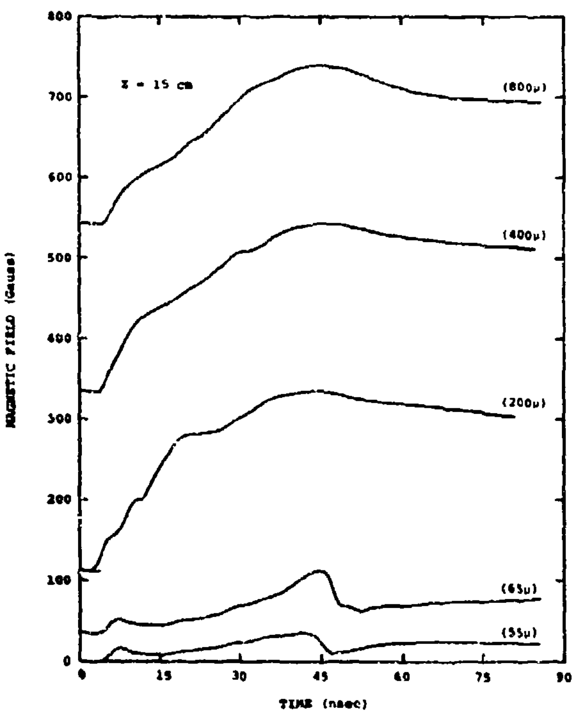

Figure 6f. Magnetic fields at Z=15 cm near chamber wall.

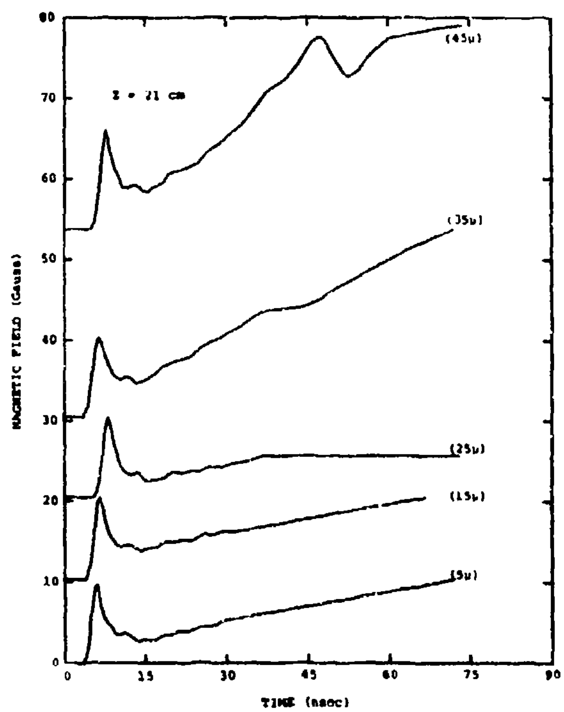

Figure 6g. Magnetic fields at Z=21 cm near chamber wall.

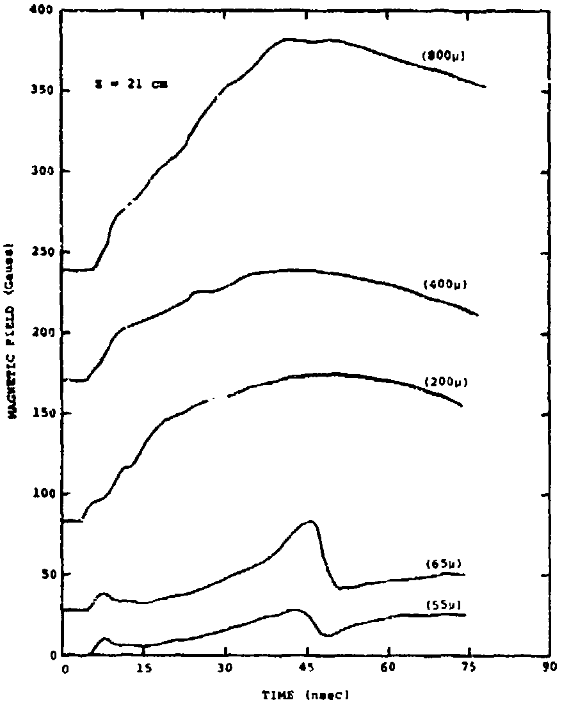

Figure 6h. Magnetic fields at z=21 cm near chamber wall

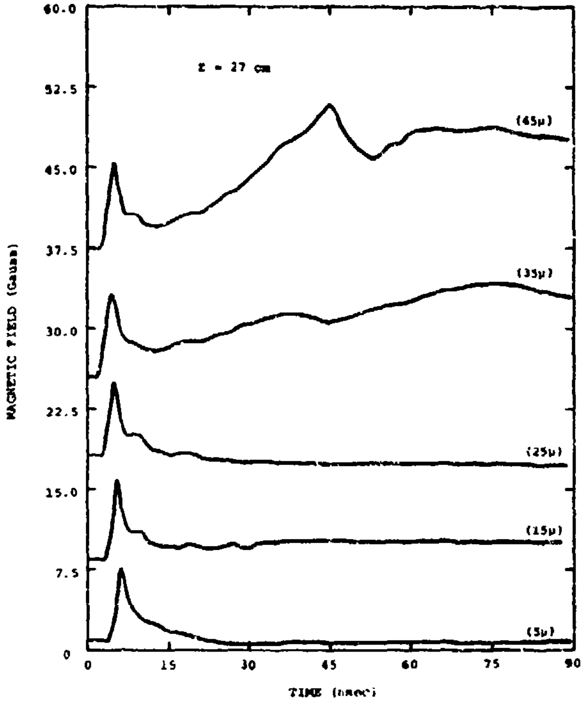

Figure 6i. Magnetic fields at z=27 cm near chamber wall.

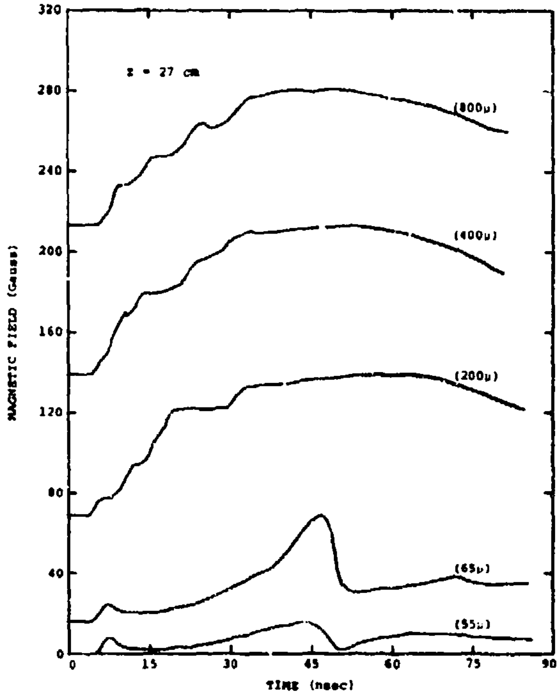

Figure 6j. Magnetic fields at z=27 cm near chamber wall.

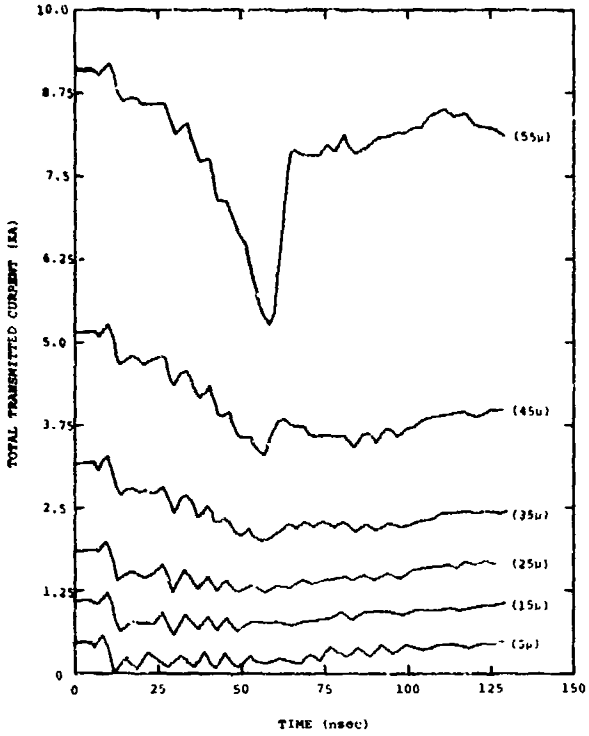

Figure 7a. Total transmitted current measured on solid endplate behind the equal-area rings.

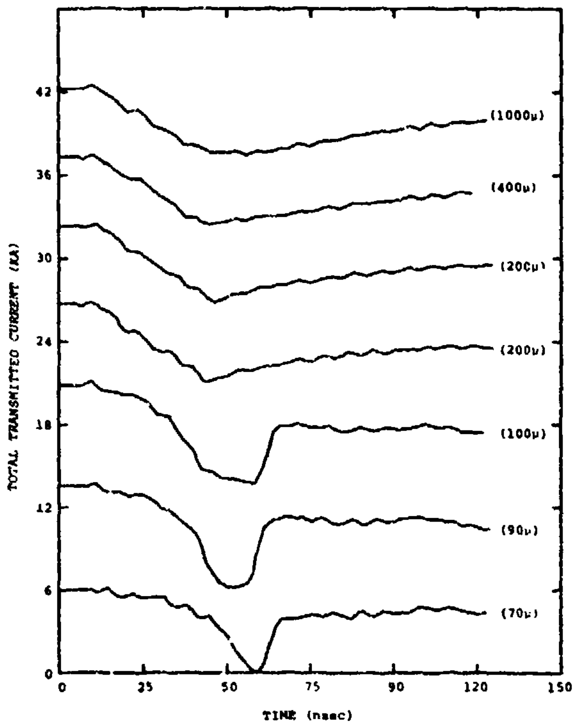

Figure 7b. Total transmitted current measured on solid endplate behind the equal-area rings.

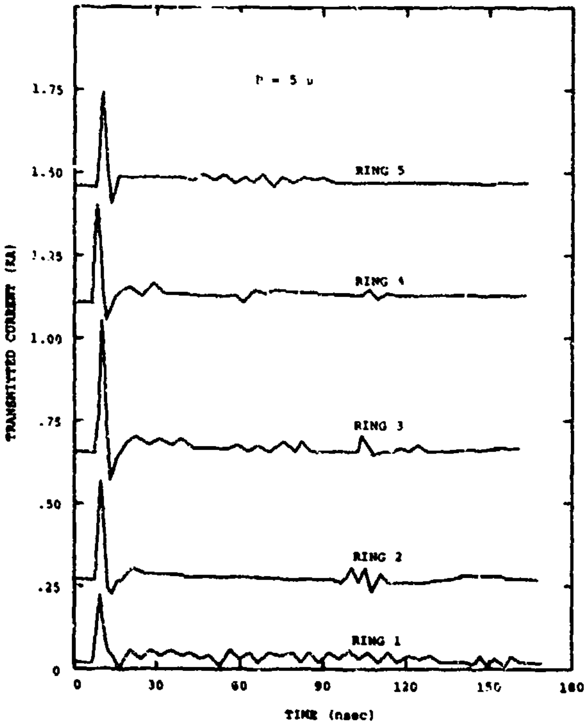

Figure 8a. Transmitted current measured on equal-area rings.

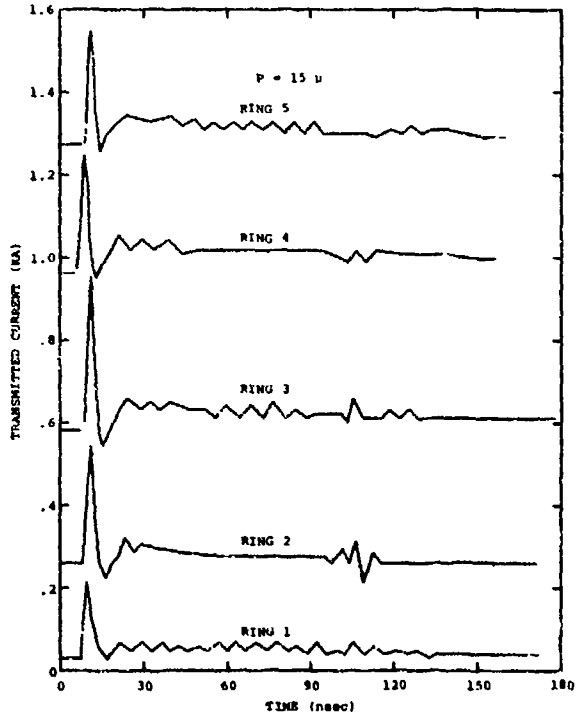

Figure 8b. Transmitted current measured on equal-area rings.

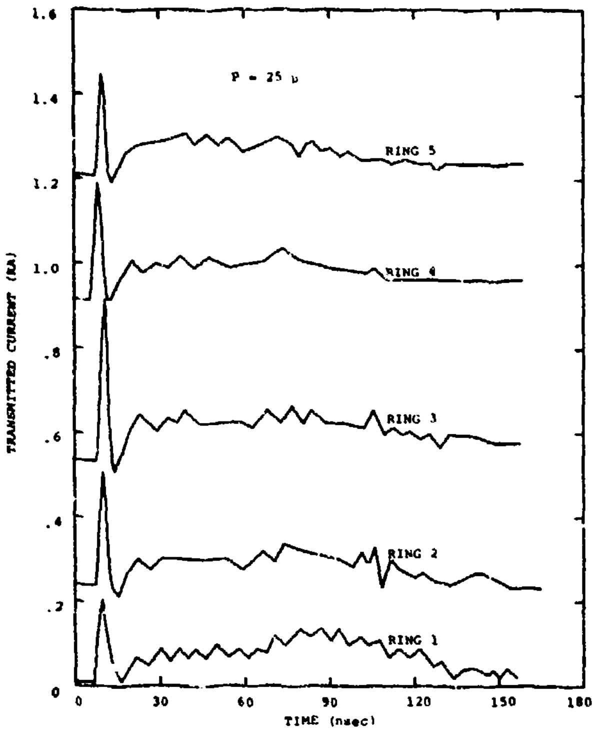

Figure 8c. Transmitted current measured on equal-area rings.

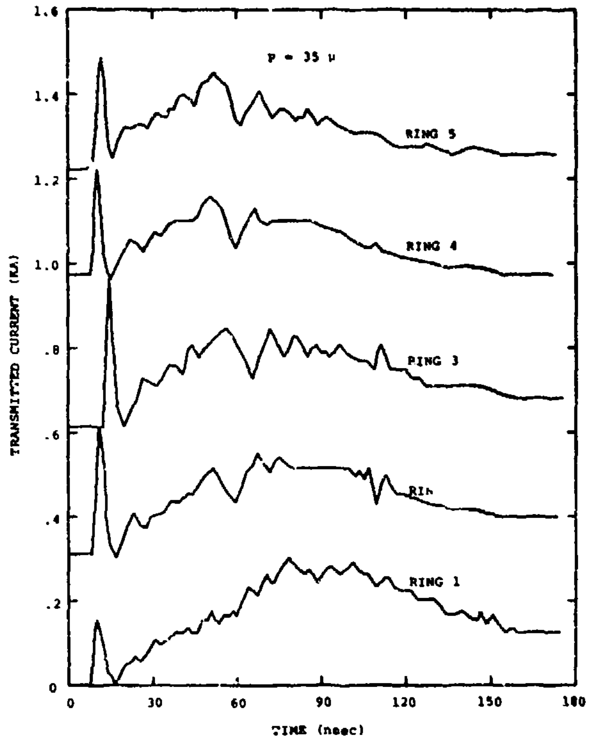

Figure 8d. Transmitted current measured on equal-area rings.

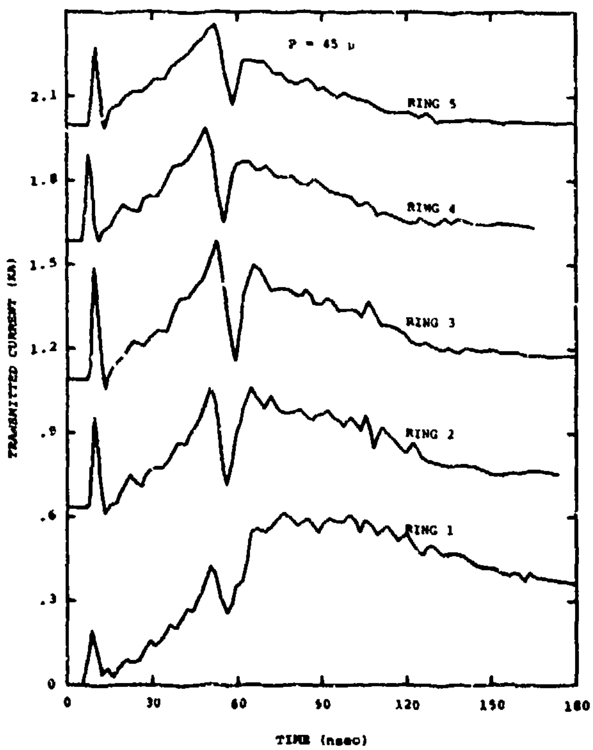

Figure 8e. Transmitted current measured on equal-area rings.

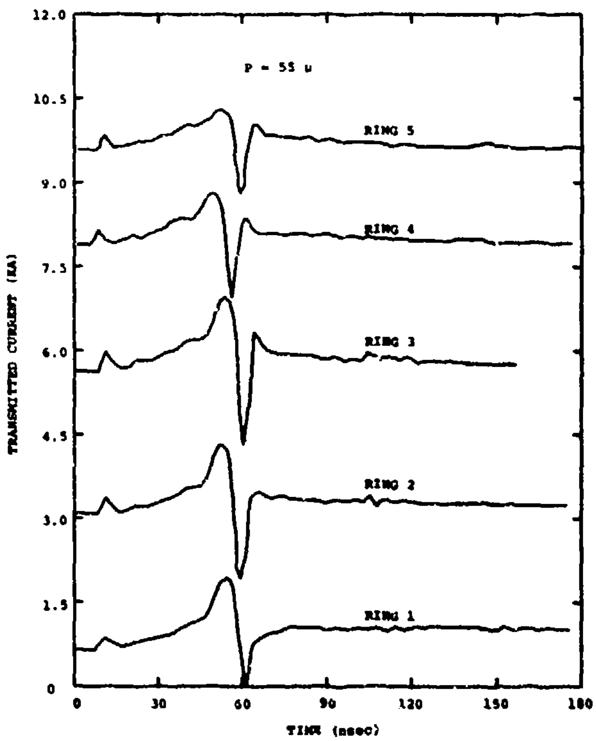

Figure 8f. Transmitted current measured on equal-area rings.

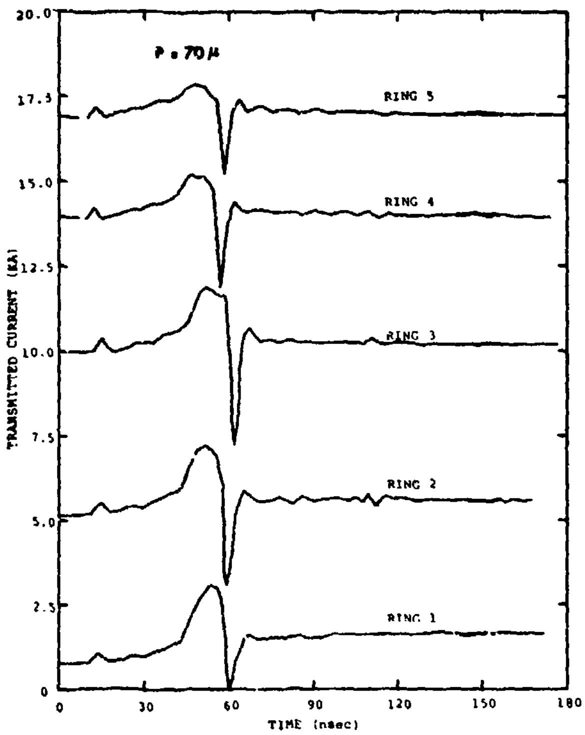

Figure 8g. Transmitted current measured on equal-area rings.

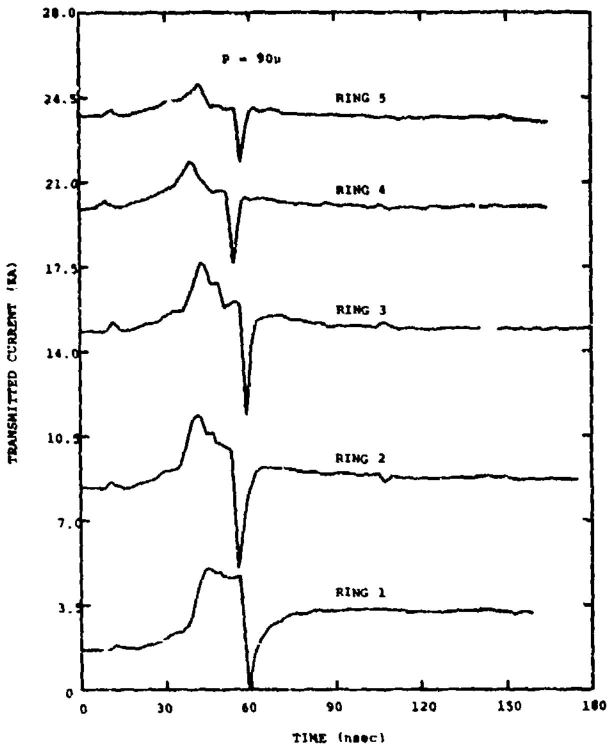

Figure 8h. Transmitted current measured on equal-area rings.

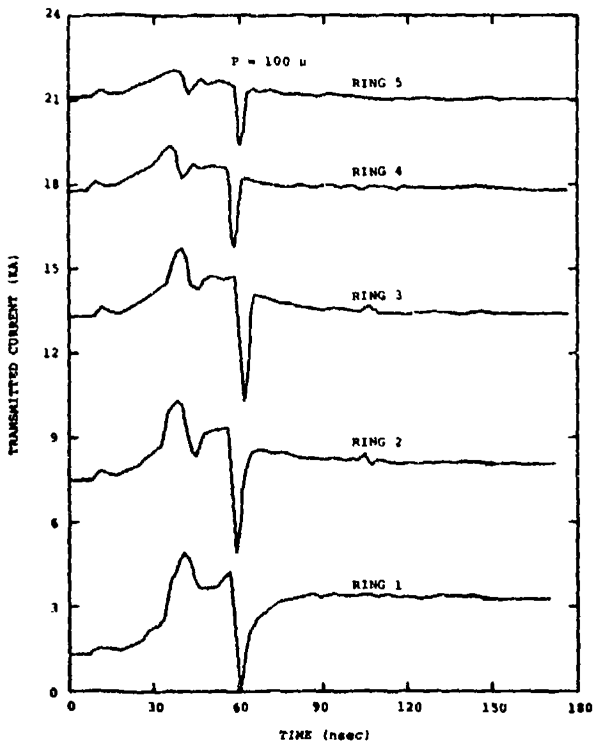

Figure 8i. Transmitted current measured on equal-area rings.

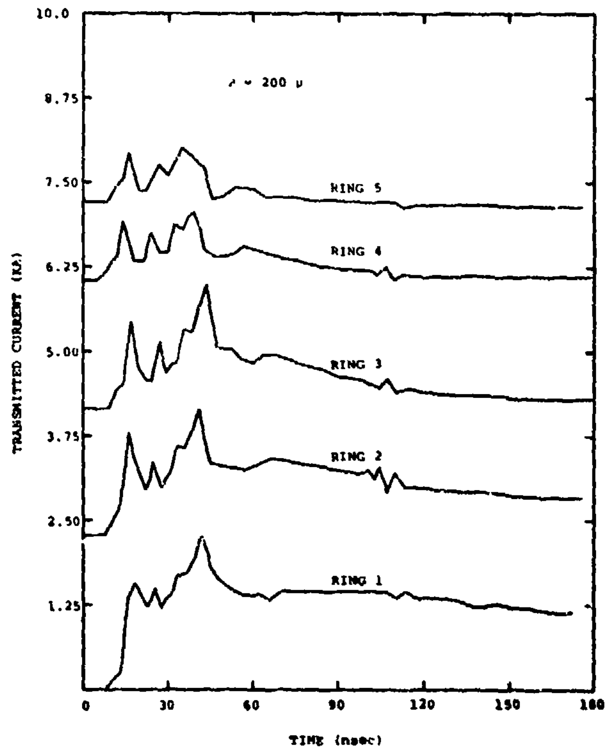

Figure 8j. Transmitted current measured on equal-area rings.

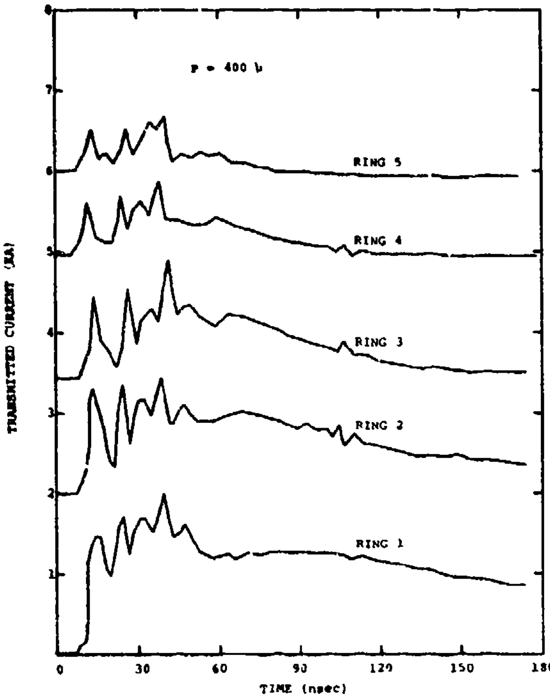

Figure 8k. Transmitted current measured on equal-area rings.

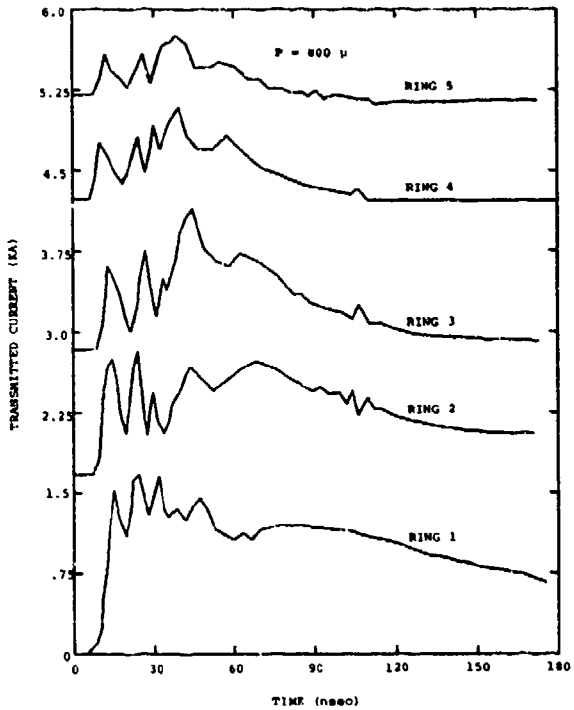

Figure 8l. Transmitted current measured on equal-area rings.

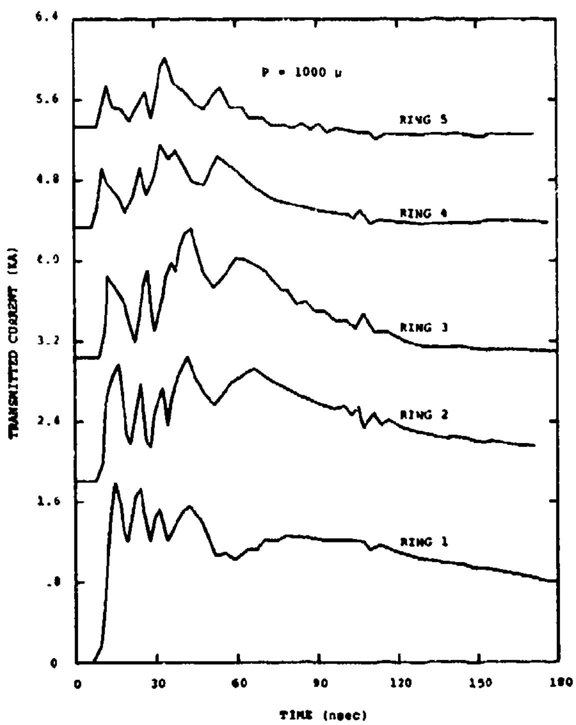

Figure 8m. Transmitted current measured on equal-area rings.

TABLE I. Chamber Endplate Current Ring Geometry

RING NO.	RADII (cm)	
	INNER	OUTER
1	-	6.7
2	6.8	9.5
3	9.6	11.7
4	11.8	13.6
5	13.7	15.0

Collected Wall Currents

The segmented-chamber-body construction of the test chamber described in reference (1) allows the monitoring of total current flowing in the chamber wall at five successive locations down the length of the cavity. The subtraction of the signal developed across the resistive gasket material in one section from that immediately nearer the injection end of the chamber yields the net current collected on the wall segment in question. Thus the average radial currents over 6 cm segments are sampled at five locations down the length of the chamber. Table II summarizes the locations of the various sections. These results are presented in Figures 9a through 9j.

TABLE II. Locations of Wall Segments. Z = 0 represents the injection plane.

Wall Segment No.	Channels Subtracted	Z Location (cm)	
		From	To
1	22A - 15A	0	6
2	15A - 16A	6	12
3	16A - 17A	12	18
4	17A - 18A	18	24
5	18A - 19A	24	30

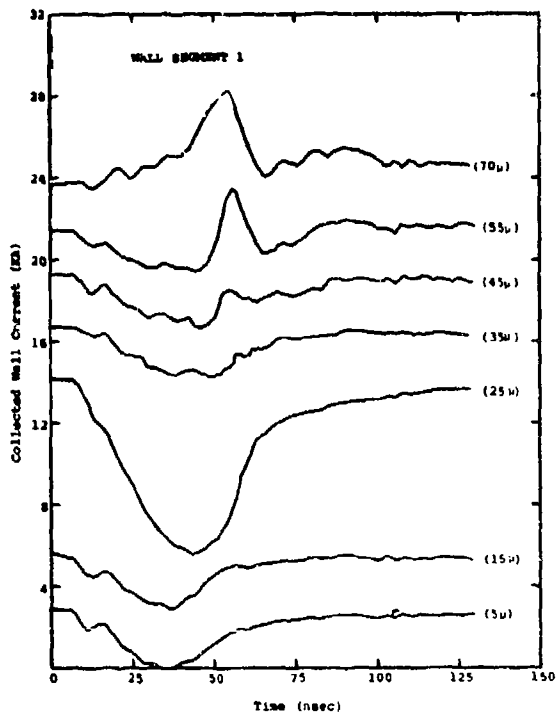

Figure 9a. Wall currents collected on segmented-chamber elements.

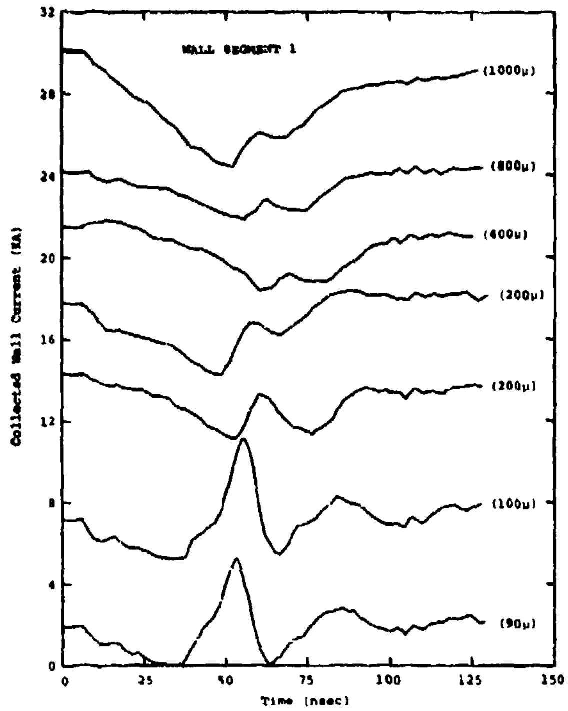

Figure 9b. Wall currents collected on segmented-chamber elements.

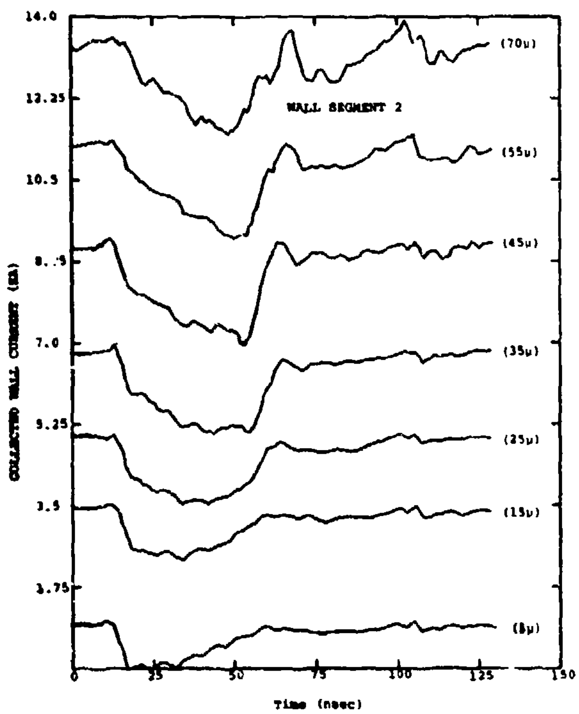

Figure 9c. Wall currents collected on segmented-chamber elements.

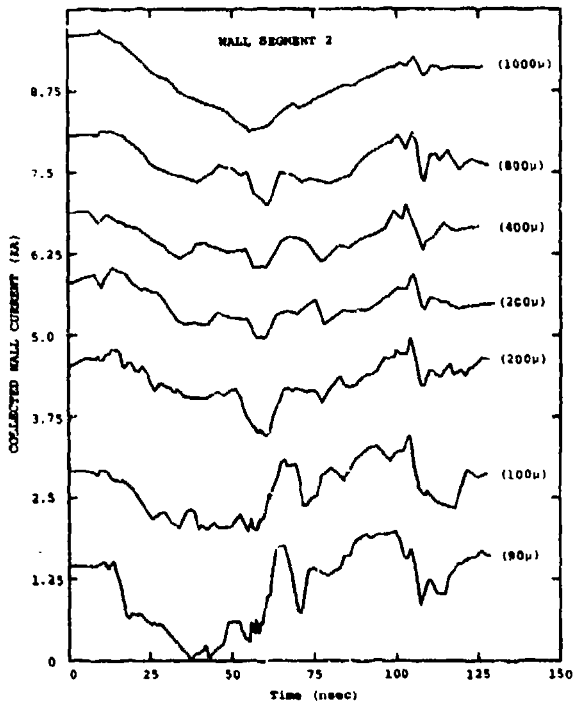

Figure 9d. Wall currents collected on segmented-chamber elements.

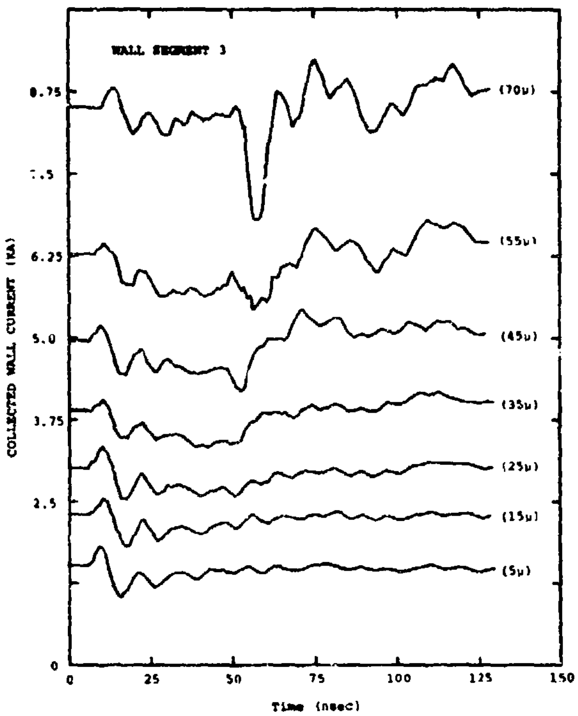

Figure 9e. Wall currents collected on segmented-chamber elements.

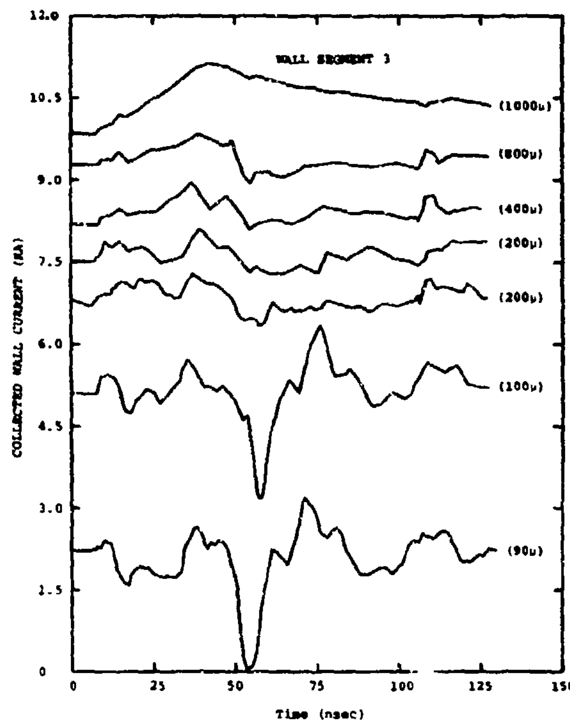

Figure 9f. Wall currents collected on segmented-chamber elements.

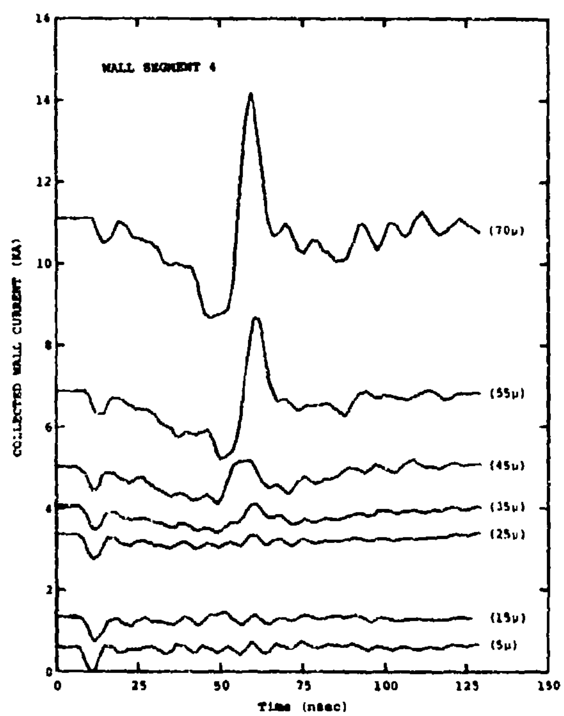

Figure 9g. Wall currents collected on segmented-chamber elements.

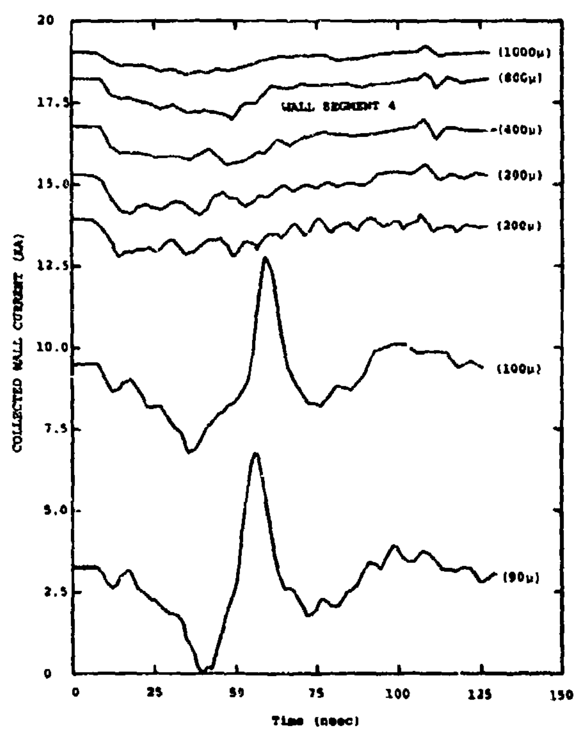

Figure 9h. Wall currents collected on segmented-chamber elements.

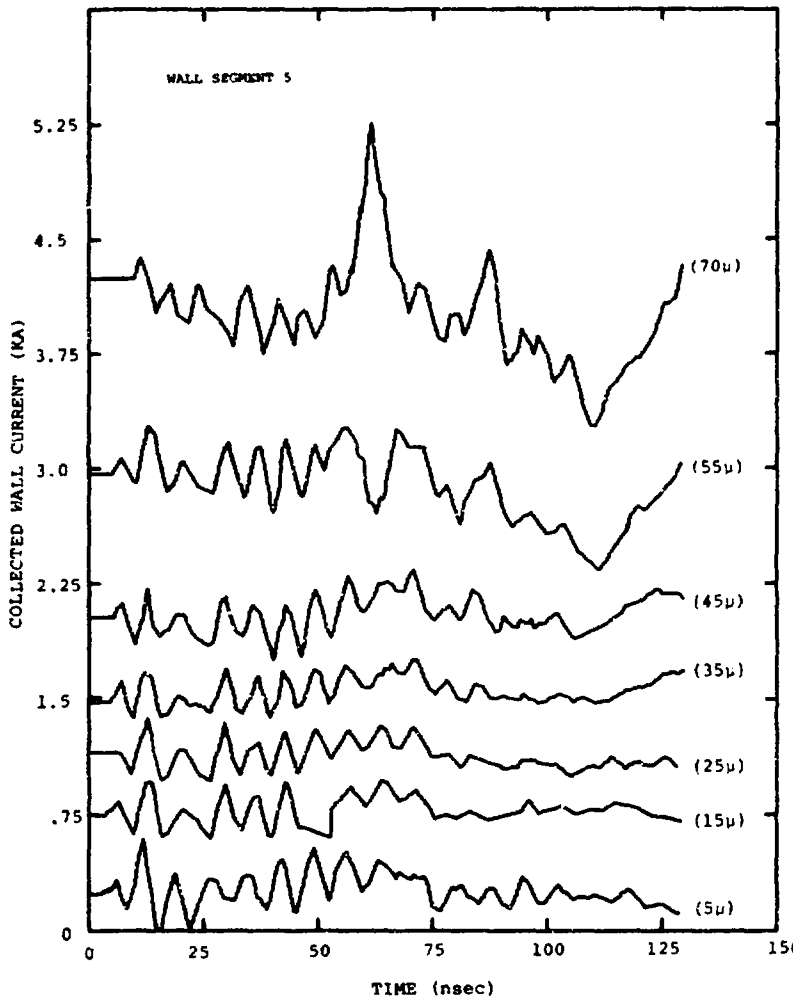

Figure 9i. Wall currents collected on segmented-chamber elements.

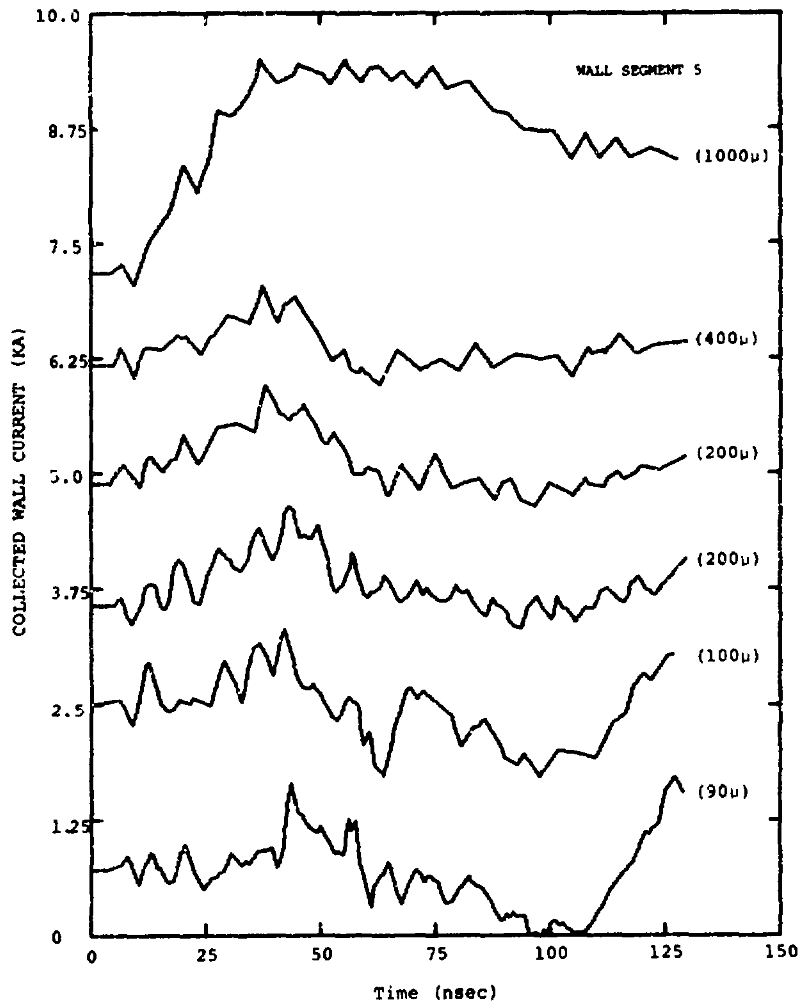

Figure 9j. Wall currents collected on segmented-chamber elements.

Radial Current Densities

An additional set of measurements were performed in the 40 keV sequence. These consisted of sampling the radial currents at seven localized points by means of flush-mounted current probes (FMCP) mounted in the chamber wall. Since these probes were employed only in the 40 keV shot sequence, a discussion of the probe construction and response is included in this report as an Appendix. The response analysis discussed therein indicates that the FMCP is an excellent device for sampling the impinging current densities. Figures 10a through 10j present data obtained using these sensors. We have elected to display these data on the same time scales as the wall segment currents to facilitate comparison of their wave shapes.

IV. PEAK VALUES

Figure 11 displays peak magnetic field values measured at $Z = 3$, 15 and 27 cm, that is, near the entrance, middle and end of the drift chamber. These data are plotted as a function of pressure.

Figure 12 similarly presents the peak values of total transmitted current against pressure. In Figure 13 are curves of collected wall current peak values for chamber sections near the front, middle and rear of the test chamber.

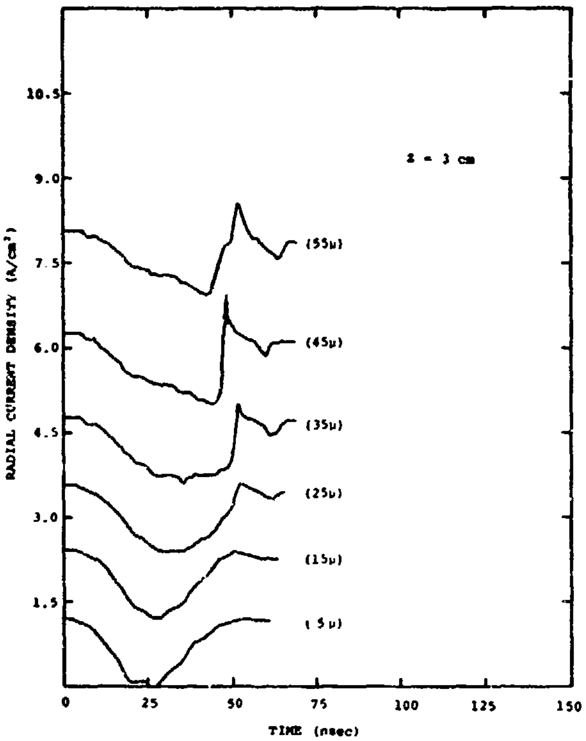

Figure 10a. Radial current density measured by the flush-mounted current probes (FMCP).

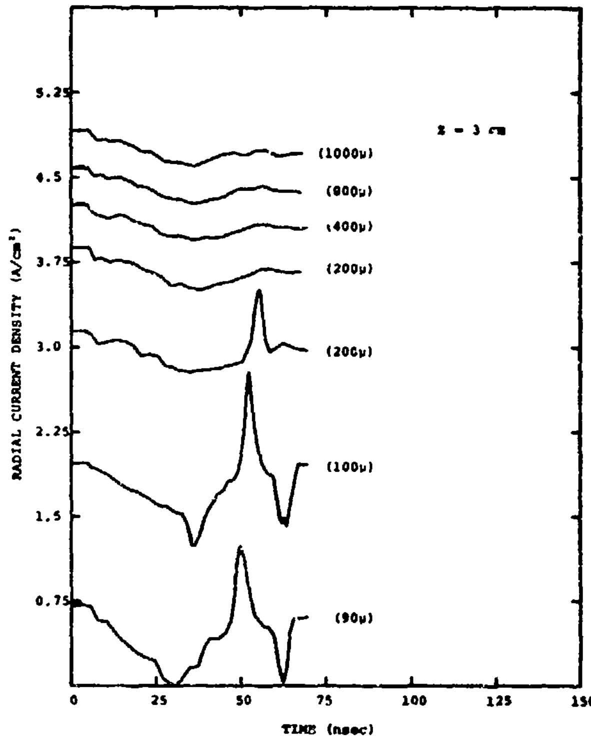

Figure 10b. Radial current density measured by the flush-mounted current probes (FMCP).

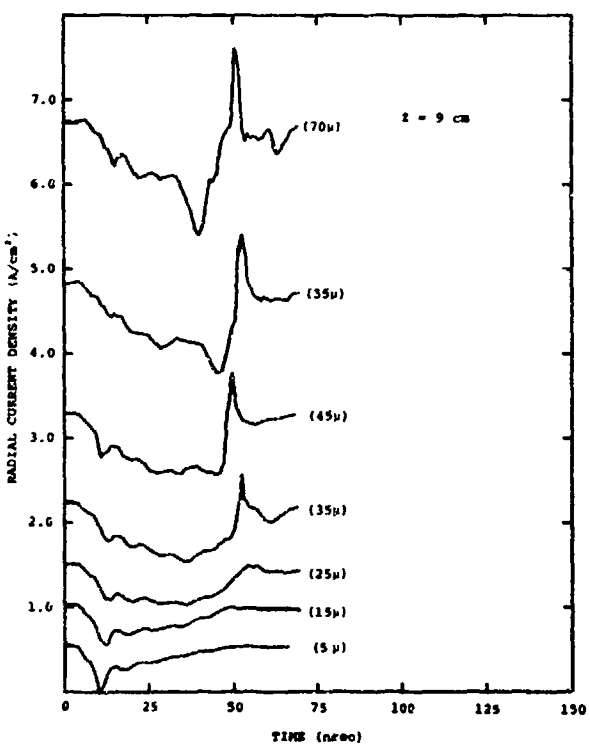

Figure 10c. Radial current density measured by the flush-mounted current probes (FMCP).

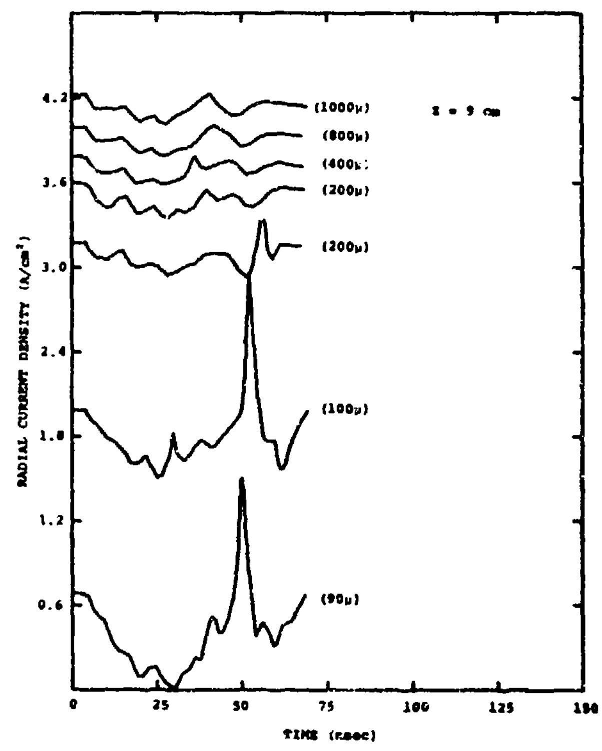

Figure 10d. Radial current density measured by the flush-mounted current probes (FMCP).

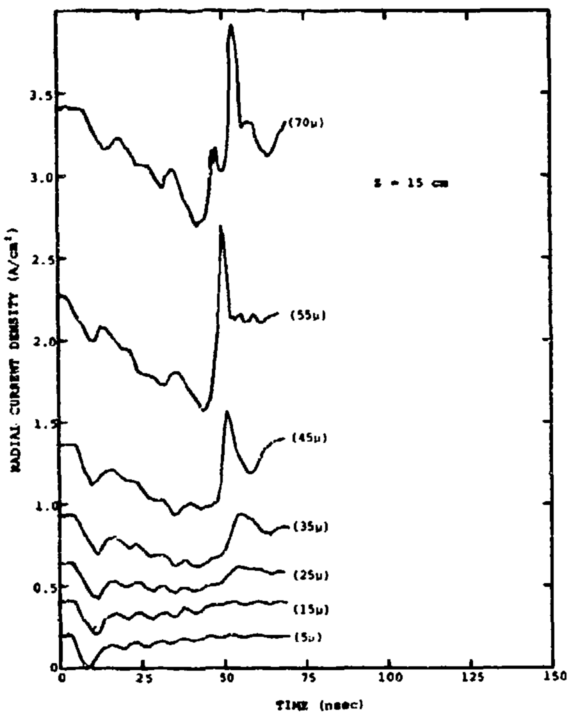

Figure 10e. Radial current density measured by the flush-mounted current probes (FMCP).

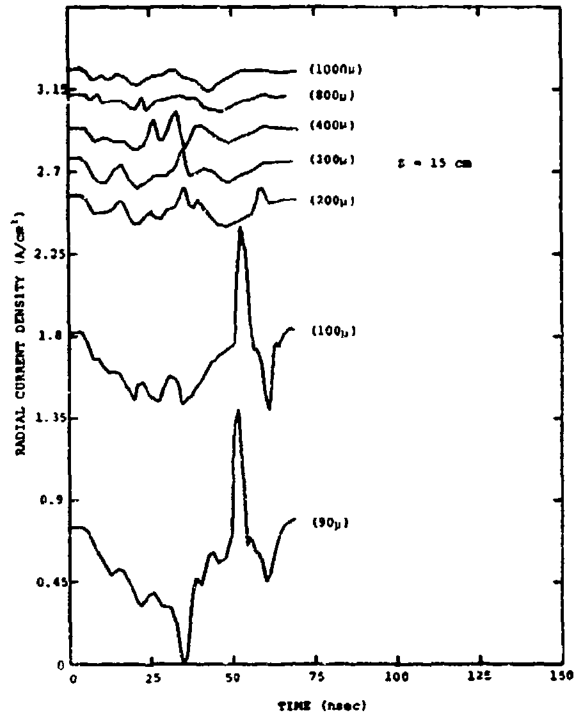

Figure 10f. Radial current density measured by the flush-mounted current probes (FMCP).

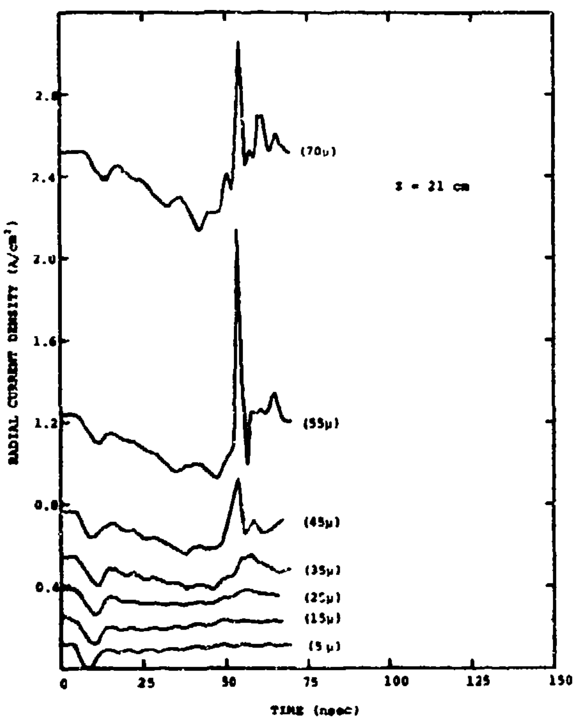

Figure 10g. Radial current density measured by the flush-mounted current probes (FMCP).

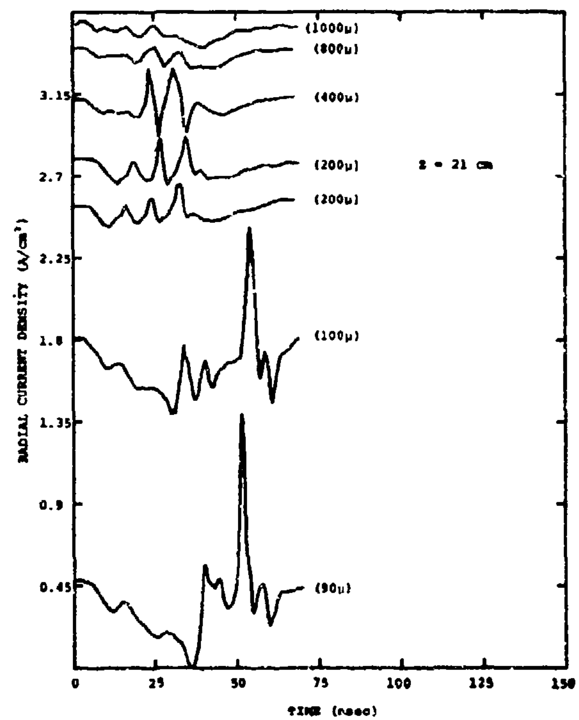

Figure 10h. Radial current density measured by the flush-mounted current probes (FMCP).

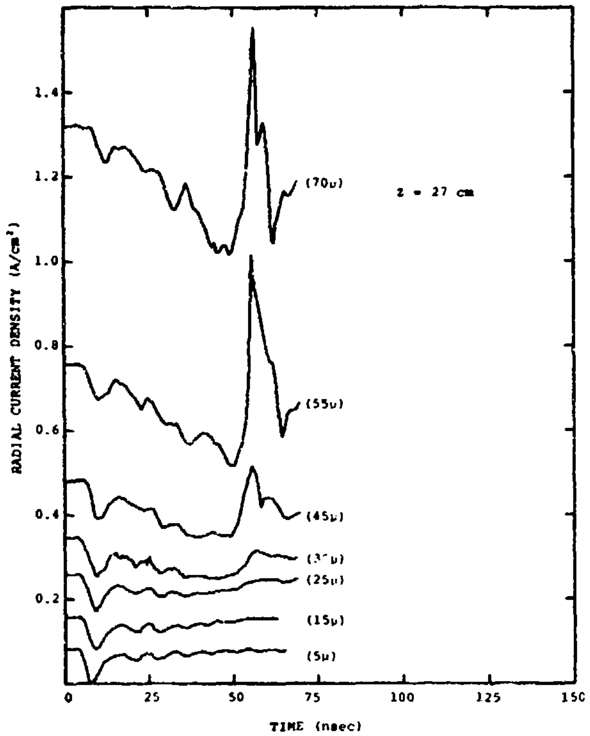

Figure 10i. Radial current density measured by the flush-mounted current probes (FMCP).

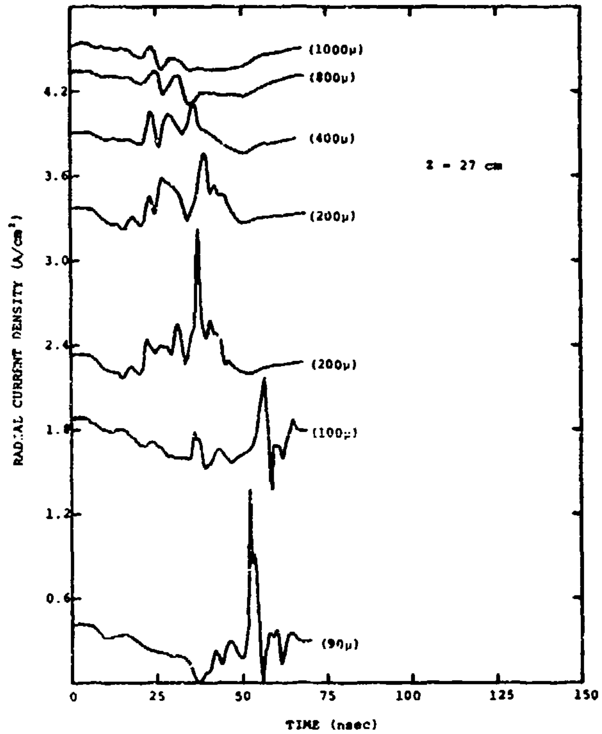

Figure 10j. Radial current density measured by the flush-mounted current probes (FMCP).

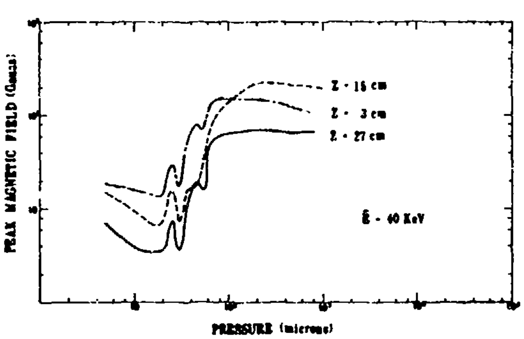

Figure 11. Peak magnetic fields vs pressure near front, middle and rear of chamber.

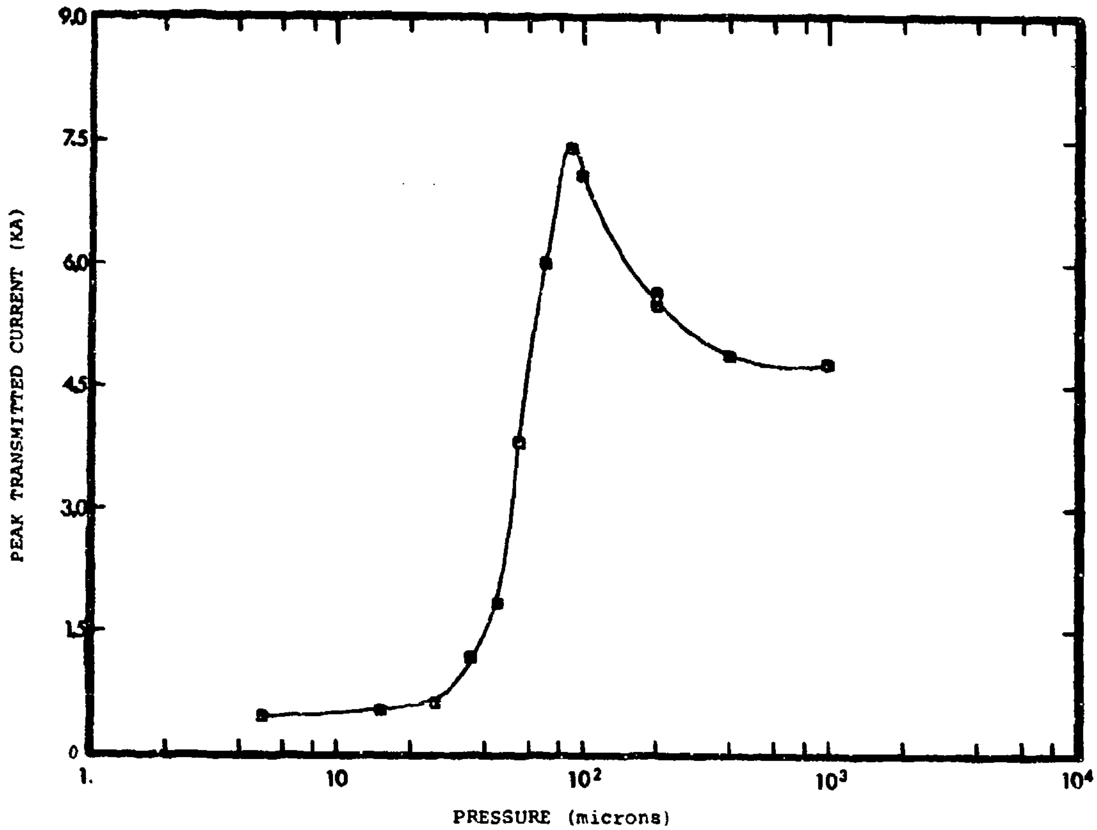

Figure 12. Peak Transmitted current vs pressure.

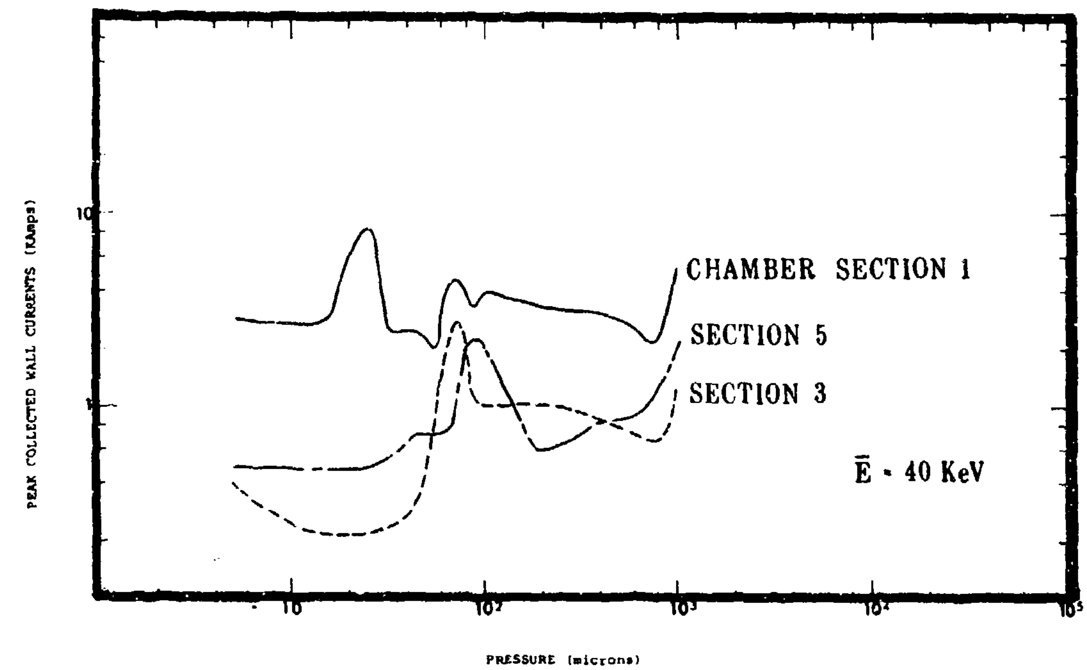

Figure 13. Peak collected wall currents near front, middle and rear of chamber

Table III summarizes the transmitted current distributions as obtained from the peak values of collected current on each of the individual endplate rings.

TABLE III. Peak currents on endplate collector rings.

Pressure (μ)	Peak Current (kA)				
	Ring 1	Ring 2	Ring 3	Ring 4	Ring 5
5	.03	.02	.04	.04	.03
10	.05	.04	.05	.05	.05
15	.03	.04	.04	.06	.06
20	.07	.06	.07	.07	.07
25	*	.06	.05	.06	.05
30	.12	.09	.10	.09	.09
35	.15	.13	.13	.09	.12
45	.56	.39	.36	.30	.28
55	.52	.41	.44	.35	.28
65	1.31	1.16	1.19	.88	.79
200	2.54	1.92	1.67	.91	.73
400	2.31	1.60	1.39	.98	.74
800	1.81	1.28	1.12	.76	.58

* Bad data film.

V. ERROR ANALYSIS

General Considerations

Sources of error have been divided into three categories: experimental error, trace digitization error and propagation of these two error types in subsequent processing. The third area of concern deals with the sensitivity of the final results to inaccuracies in the input data.

Conversion of Oscilloscope Traces to Volts vs Time

In order to set the time scale on each scope, a sine wave of known frequency was recorded on each channel photograph prior to each shot. The distance (from an arbitrary zero point) to each successive peak of this waveform was digitized. From these data the mean μ' and standard deviation σ' of the distances $x_{i+1}-x_i$, $i = 1, 2, \ldots, n$ between successive peaks were computed.

Let X be the random variable associated with distance errors in the digitized x (time) axis. We assume that X has mean 0 and variance σ^2. Let μ be the "actual" sine wave inter-peak distance, then X_i will be distributed as $X + i\mu$. Hence $X_{i+1} - X_i$ will have mean μ and variance $2\sigma^2$ given independence of X_i and X_{i+1}.

The statistic μ' was used to estimate μ and $\frac{\sigma'}{\sqrt{2}}$ was used to estimate σ. σ' was found to be less than .036 mm on nearly every shot. Other sources of error, such as non-uniformity of the sine wave, have been ignored. These sources would cause a slight under-estimate of data quality rather than an over-estimate. It is assumed that

voltage errors (vertical distances) are distributed the same as time errors (horizontal distances).

Voltage values are calculated from the raw digitized data as:

$$v = \frac{(d-d_o)\,a\,s}{m}$$

where:

- d is the vertical coordinate of the trace on the film (mm)
- d_o is the vertical coordinate cooresponding to 0 (mm)
- m is an optical magnification factor associated with the digitizing process
- a is signal attenuation, and
- s is scope sensitivity $\left(\frac{v}{mm}\right)$.

Relativising voltage errors ΔV to the peak voltage encountered $|V|_{max}$, one obtains

$$\sigma\left(\frac{\Delta V}{|V|_{max}}\right) = \sqrt{\sigma^2\left(\frac{\Delta(d-d_o)}{|d-d_o|_{max}}\right) + \sigma^2\left(\frac{\Delta a}{a}\right) + \sigma^2\left(\frac{\Delta s}{s}\right) + \sigma^2\left(\frac{\Delta m}{m}\right)}\ .$$

$\sigma\left(\Delta\left(d-d_o\right)\right)$ was approximated by .036 mm (see above) and $|d-d_o|_{max}$ was tabulated for a sample of curves from each type of data.

In all curves investigated

$$\sigma\left(\frac{\Delta\left(d-d_o\right)}{|d-d_o|_{man}}\right) < 5.5\% \quad .$$

Other values assigned were:

$$\sigma\left(\frac{\Delta a}{a}\right) = 1\%$$

$$\sigma\left(\frac{\Delta s}{s}\right) = 2\%$$

$$\sigma\left(\frac{\Delta m}{m}\right) = .05\%$$

Hence $\sigma\left(\frac{\Delta V}{|V|_{max}}\right) \approx 6\%$ which represents the error inherent in the digitized data upon which all further processing was performed.

Transmitted Current Measurements (Total and Radially Resolved)

These measurements result from measuring voltages developed across resistive shunts and therefore involve application of Ohm's Law in the form $I = V/R$. Percentage errors associated with peak values were evaluated according to the following procedures.

Letting ΔI, ΔV and ΔR denote random variables corresponding to current, voltage and resistance errors respectively with variances $\sigma^2(\Delta I)$, $\sigma^2(\Delta V)$ and $\sigma^2(\Delta R)$, one obtains

$$\sigma\left(\frac{\Delta I}{|I|_{max}}\right) \cong \sqrt{\sigma^2\left(\frac{\Delta V}{|V|_{max}}\right) + \sigma^2\left(\frac{\Delta R}{R}\right)} \quad .$$

As determined in the preceeding section, $\sigma\left(\frac{\Delta V}{|V|_{max}}\right) = .06$. The worst case $\sigma\left(\frac{\Delta R}{R}\right)$ for the channels under consideration in this section was about .05. Hence $\sigma\left(\frac{\Delta I}{|I|_{max}}\right) < 8\%$ for the total transmitted current measurements. Recent considerations relative to interpretation of the current collection ring data, however, has indicated that the response of these rings is not well understood. The antenna mode response of the concentric ring configuration appears to be greater than originally determined. It is not possible at this time, therefore, to complete the error analysis of those sensors.

Wall Segment Currents

The net wall current in each of the five sections comprising the body of the drift chamber is computed as $v_2(t)/r_2 - v_1(t)/r_1$ where $v_1(t)$ and $v_2(t)$ are the digitized voltages associated with two successive sections and r_1 and r_2 are the corresponding gasket resistances. The error analysis here is complicated by the fact that relative timing discrepancies between the two voltage waveforms must be accounted for.

Timing errors in a given trace are assumed to be of two kinds. The first is a systematic error. That is, due to inaccurate determination of the timing zero point, the entire waveform is shifted in time with respect to true zero and hence with respect to the waveform with which it is to be differenced. The second error source is a random inaccuracy in the determination of the time of each individual data point. It was judged that these random errors were quite small leaving the systematic error of the first type dominant.

To analyse the effect of the systematic timing errors, let $i_1(t)$ and $i_2(t)$ be correct current values whose difference $i_2(t) - i_1(t)$ is desired. Due to errors of various sorts, $i_2'(t)$ is obtained instead of $i_2(t)$ and $i_1'(t)$ instead of $i_1(t)$. Allow a relative time shift error of a = 2.5 nsecs and assume that there exist time shifts S_1 and S_2 such that $|S_k|<a$ and $|i_k(t)-i_k'(t+S_k)|<\varepsilon_k$ for k = 1,2 and all t of interest. In other words, assume that $i_k'(t)$ time-shifted by a small amount S_k is a good approximation to $i_k(t)$. Define $b_k(t) = \max\limits_{|s|\leq a} |i_k'(S+t)-i_k'(t)|$ then $|i_k'(S+t)-i_k'(t)|\leq b_k(t)$ for $|S|< a$. Hence $b_k(t)$ is the maximum amount that $i_k'(t)$ can vary as it is time-shifted by amounts varying from -a to a.

The difference between the calculated value and the desired result $i_2(t) - i_1(t)$ is of interest. The triangle inequality yields:

$$|i_2'(t)-i_1'(t)-(i_2(t)-i_1(t))|$$

$$\leq|i_2'(t)-i_2'(S_2+t)|+|i_2'(S_2+t)-i_2(t)|+|i_1'(t)-i_1'(S_1+t)|+|i_1'(S_1+t)-i_1(t)|$$

$$\leq b_2(t) + \varepsilon_2 + b_1(t) + \varepsilon_1$$

The bound $b_k(t)$ measures the local variation in $i_k'(t)$ and will vary with t. In simplest terms, small time shifts will cause dramatic changes in $i_k'(t)$ where $b_k(t)$ is large and $i_k'(t)$ has steep slopes.

In a number of cases including high and low pressures, $b_k(t)$ was computed for a = 2.5 ns, k = 1, 2 and t corresponding to the maximum of $|i_2'(t)-i_1'(t)|$. $b_1(t) + b_2(t)$ was found to be less than 0.7 kA in nearly every case. Assigning standard deviations of 0.4 kA to ε_1 and ε_2 one obtains a standard deviation of 0.9 kA for the total error. The estimate is believed to be conservative in the sense that it bounds the true standard deviation but that 0.6 kA is probably a more realistic estimate.

Magnetic Fields

The magnetic field results were calculated from the moebius loop data using the formula:

$$B(t) = \frac{L}{2AR}\left\{ v(t)+\frac{R}{L}\int_0^t v(\tau)d\tau \right\}$$

where:

$A = (1.08 \pm .01) \times 10^{-4} m^2$

$R = 25\Omega$

$L = (16.9 \pm .01) \times 10^{-9} hy$

v(t) is the digitized voltage trace corrected for data channel attenuations. That is, v(t) represents the output voltage of the sensor itself.

The presence of errors in v(t) can be handled by replacing v(t) with $v(t)+\varepsilon(t)$ where $\varepsilon(t)$ is an error term. Define

$$B^*(t) = \frac{L}{2AR}\left\{v(t)+\varepsilon(t)+\frac{R}{L}\int_0^t \Big(v(\tau)+\varepsilon(\tau)\Big)\,d\tau\right\} .$$

Hence,
$$|B^*(t)-B(t)| = \left|\frac{L}{2AR}\left\{\varepsilon(t)+\frac{R}{L}\int_0^t \varepsilon(\tau)\,d\tau\right\}\right|$$

$$= \leq \frac{L|\varepsilon(t)|}{2AR} + \left|\frac{1}{2A}\int_0^t \varepsilon(\tau)\,d\tau\right|$$

$$\leq \frac{L|\varepsilon(t)|}{2AR} + \frac{t}{2A}\max_{0\leq\tau\leq t}|\varepsilon(\tau)| .$$

Because errors of a small level shift and/or rotation are judged present in the process of reading the photographic images, one must allow for cumulative error rather than assuming that the error will "average out" over time. This cumulative error corresponds to the term:

$$\frac{1}{2A}\int_0^t \varepsilon(\tau)\,d\tau .$$

The following example illustrates the problem of cumulative error. Given a uniform level shift error in v(t) of 2% of its peak value, a simple computation shows that

$$\frac{1}{2A}\int_{0}^{t} \varepsilon(\tau)d\tau$$

could accumulate an error equal to the peak value of $\frac{Lv(t)}{2AR}$ in time $t = \left(\frac{1}{.02}\right)\frac{L}{R} \approx 34$ ns. At t = 34 ns it would not be uncommon to find values of B*(t) of roughly this same magnitude.

In summary, the values calculated for B(t) decrease in accuracy with advancing time and can be rather unreliable even at times as early as 35 ns. The values for B(t) at times near zero approach the accuracy of the digitized voltages since the errors in A, R and L are small.

What this means in practice for this set of data in which both the signal levels are small and pulse durations are short is that in those magnetic fields for which the peak values occur beyond 40 nsec, the peak values are not very reliable. It is estimated that a bound on the error on the computed value of the B fields is probably between 50 and 75% at 40 nsec. There is evidence, however, that the error is not nearly that bad in much of the data; but quantifying it in each case is extremely difficult. One reason for believing the error is much less is that on many shots in which there are three loops azimuthally distributed at given Z coordinate, the resulting calculated B fields agree to within 15%. In other cases the disagreement is marked, and a late time ramp attributable to a fixed zero offset in the raw data is apparent.

Attempts to simply subtract out the associated zero were not satisfactory and it was felt that further tinkering with the data to produce better "agreement" was scientifically unwarranted.

It should be noted that the 60 and 125 keV data sets have much less error associated with them. This is due to two factors. First those data have significantly better signal-to-noise characteristics in that the signals are of both greater amplitude and longer pulse duration. Secondly, the digitizing of those data was performed using much more accurate equipment and processes than the present set.

Flush-Mounted Current Probes

The formula $J_r(t) = K_1 v(t) + K_2 \frac{dv(t)}{dt}$ was used to calculate the radial current densities from the flush-mounted current probe voltage data with $K_1 = 129.9$ and $K_2 = 158.4$. (See Appendix.) The derivative $\frac{dv}{dt}$ at t_2 was approximated by evaluating the slope of a parabola passing through $(t_1, v(t_1))$, $(t_2, v(t_2))$ and $(t_3, v(t_3))$ where t_1, t_2 and t_3 are consecutive time points. A new parabola was fit to successive sets of three points advancing along the data points one at a time.

Here the sensitivity of the derivative calculation to errors in the input data is of over-riding concern. The result $J_r(t)$ is least sensitive to errors in $v(t)$ when either the term $\frac{dv}{dt}$ is small or the term $K_2 \frac{dv}{dt}(t)$ is at least small with respect to the term $K_1 v(t)$.

In order to evaluate the sensitivity of the derivative calculation to errors in the input times, the derivative was written as a function $g(t_1,t_2,t_3,v_1,v_2,v_3)$ and the gradient ∇g was computed for actual data points. For the most part the standard deviations of the timing errors were approximately 0.25 nsec. It was found that times near the steepest part of $v(t)$ could yield errors exceeding 20% of the resulting $J_r(t)$ peak value even though the time error $(\Delta t_1,\Delta t_2,\Delta t_3)$ satisfied the requirement $((\Delta t_1)^2+(\Delta t_2)^2+(\Delta t_3)^2)^{\frac{1}{2}} < 0.25$ nsec. The derivative computation is a good deal less sensitive to errors in $v(t)$ where $v(t)$ is steep. At times when the curve $v(t)$ flattens out, the accuracy of the $J_r(t)$ values approaches the accuracy of $v(t)$.

In summary, the flush-mounted current probe data has an error bound of about 20% but is probably routinely good to 10%.

APPENDIX A

FLUSH-MOUNTED CURRENT PROBE

The flush-mounted current probes (FMCP) employed in this experiment were designed to measure the radial electron current density impinging on localized areas of the test chamber walls. The probes themselves consist of a current collection element which was a rod of diameter 7 mm insulated from its surrounding support structure by a 1.05 mm layer of epoxy. The entire probe assembly was inserted into the wall structure of the chamber so that the face of the probe was flush with the inside wall of the chamber and the support structure and chamber walls were common. Terminals on the collection element and the support structure provide the signal path to a 50 ohm terminated line leading directly to a Tektronix 519 oscilloscope.

There are two potential modes of excitation of the sensor which have been analysed: direct current collection of the radial component of the electron current impinging on the sensor face (the desired response) and the antenna response due to the axial component of the electric field in the vicinity of the sensor. An additional excitation mode is due to displacement currents in the vicinity of the sensor; but this mechanism is judged to be negligible and was not explicitly considered. An analysis of the probe response has been performed assuming ramp functions of appropriate slopes for the E_z and J_r driving functions based on the equivalent circuit model for the probe and its 50 ohm load shown in Figure 1-A.

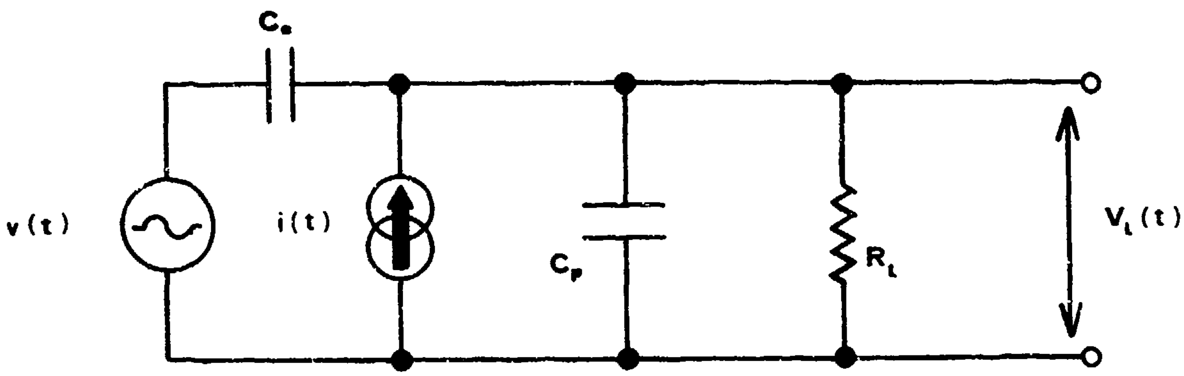

Figure 1-A. Equivalent circuit model of the flush mounted current probe.

In this Figure, v(t) represents the antenna voltage, C_a the antenna capacitance, i(t) represents the collection current on the center rod, C_p the capacitance formed by the current collection electrode and the rest of the support structure, R_L is the 50 ohm load and V_L is the measured voltage output of the probe system. The driving ramp functions were chosen to have slopes similar to the rise times of J_r and E_z observed in the experiment. Table 1 tabulates the analysis results. V_a is the response voltage at the load due to the antenna effects of the probe, V_c is that due to the impinging current and V is the total response. The table indicates that for times as early as 1 nsec, the error in attributing the entire response to the collected current is less than 3%. At later times the error becomes totally negligible. Therefore, the equivalent circuit may be simplified even further to that shown in Figure 2-A the circuit equation of which is

TABLE 1. Tabulation of Flush-Mounted Current Probe (FMCP) Analysis Results

t(ns)	V_a (volts)	V_c (volts)	$V_L(t)$ (volts)	$\left\lvert\frac{V_a(t)}{V(t)}\right\rvert$ %
0.2	.187	0.976	1.163	16.8
0.4	.212	2.570	2.782	7.7
0.6	.215	4.31	4.526	4.8
1.0	.216	7.7	7.9	2.7
2.0	.216	16.3	16.5	1.3
4.0	.216	33.5	33.7	0.6
6.0	.216	50.7	50.9	0.4
10.0	.216	85.1	85.3	0.2

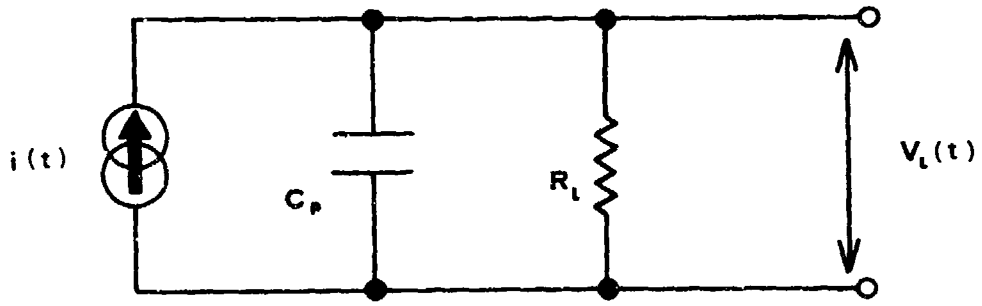

Figure 2-A. Reduced model of the flush-mounted current probe.

$$i(t) = C_p \frac{dV_L}{dt} + \frac{V_L}{R}$$

from which

$$J_r(t) = \frac{C}{A} \frac{dV_L}{dt} + \frac{V_L}{RA}$$

where A = area of the probe collection element.

Hence, inserting the proper numerical values:

$$J_r(t) = 155.8 \frac{dV_L}{dt} + 129.9\ V_L$$

where $J_r(t)$ is given in A/m^2.

APPENDIX B

INSTRUMENTATION DETAILS

In this section some additional details of the instrumentation of the test chamber not included in reference 1 are presented.

Magnetic Field Sensors

Standard moebius strip loops with potted gaps were employed as the magnetic field sensors. A good discussion of the principles of operation of the loops themselves can be found in the AFWL EMP Sensor and Simulation Note Number 7. Figure 1-B shows the data channel configuration, while Figure 2-B presents the schematic details of the balun employed. Figure 3-B is a photograph of the sensor itself. Figure 3 of reference 1 shows the loops mounted in the drift chamber walls.

Current Collection Sensors

Voltage signals proportional to current through the resistive gasket material separating the individual chamber segments were picked off directly by attaching 50Ω RG-58 cables to the chamber segment flanges. Figure 4-B illustrates this. The equal area current rings were isolated from the solid endplate also by resistive gaskets, and the voltage signals developed by collected current on each of those was similarly tapped. Resistances of each gasket were experimentally determined (reference 1, p. 18). Each ring had a signal pickup feedthrough which protruded through the chamber endplate. These signals were fed directly down the long 50Ω cables to the instrument vans where they passed through cable equalizers, delays, attenuators and terminations to the oscilloscopes. All intervening components were of course properly matched so that, from the point of view of the sensor input, the effective load was simply 50Ω.

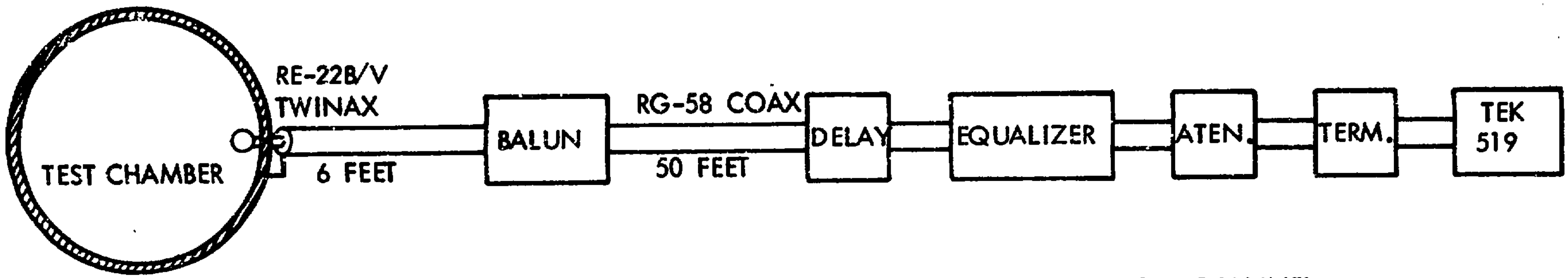

FIGURE 1-B MOEBUS LOOP DATA TRANSMISSION CHANNEL

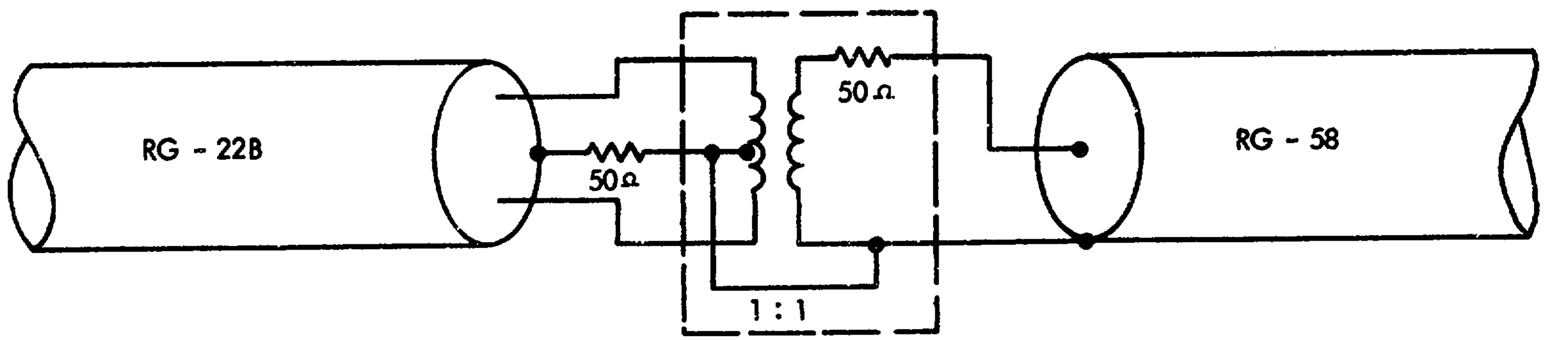

VARI-L 100100C WIDEBAND TRANSFORMER

FIGURE 2-B BALUN TERMINATION ELECTRICAL SCHEMATIC

Figure 3-B. Moebius loop magnetic field sensor.

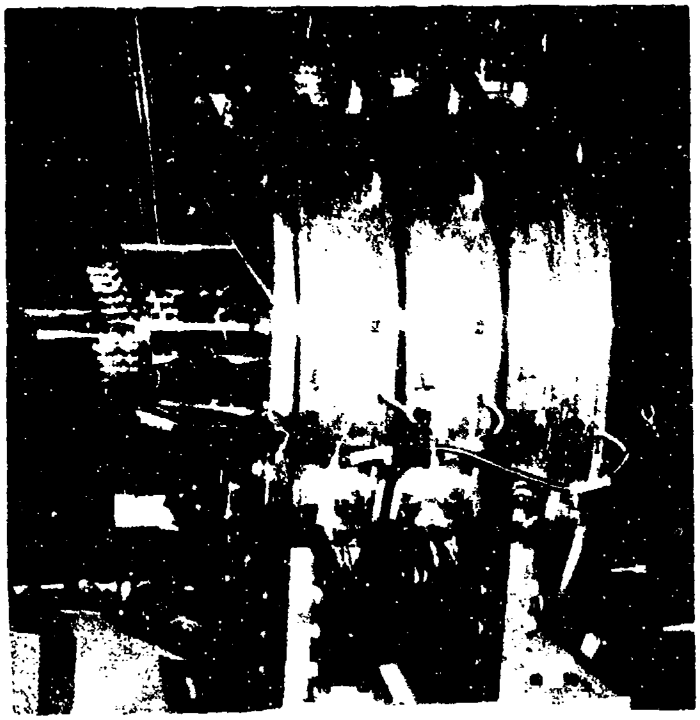

Figure 4-B. External connections of wall segment signal pickups.

Flush-Mounted Current Probes

The flush-mounted probes for measuring the radial current density are discussed in Appendix A. Figure 5-B is a photograph of one of the sensors. The output was tapped by direct connection of a 50Ω cable to two screw terminals on the back of the sensor mount itself. This signal was fed down the cable to the instrument van where it passed through components similar to those discussed in the previous paragraph for the current collection sensors. The effective load on each flush-mounted probe was 50Ω.

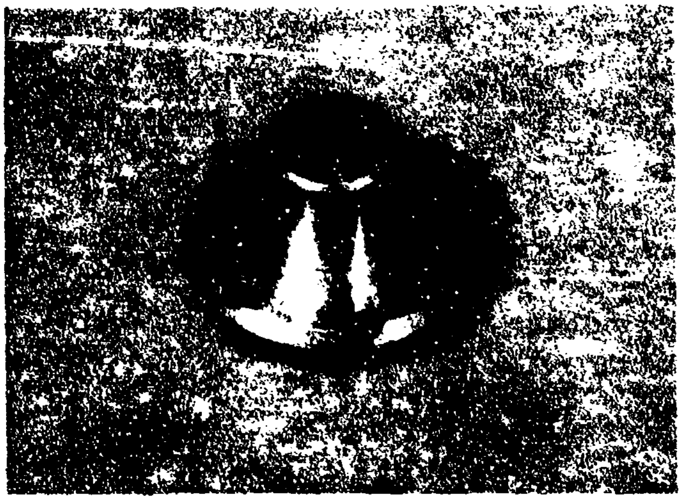

Figure 5-B. Photograph of sensor.

DISTRIBUTION LIST

DEPARTMENT OF DEFENSE

Director
Defense Advanced Research Projects Agency
ATTN: NMR

Director
Defense Civil Preparedness Agency
ATTN: TS AED

Defense Communication Engineer Center
ATTN: Robert Rostrom
ATTN: Code R-103P
ATTN: Code 1035, Nicholas A. Sica

Director
Defense Communications Agency
ATTN: Code 930, Monte I. Burgett, Jr.
ATTN: Code B-205, George B. Adkins
ATTN: Code 430
ATTN: Code 800, Fred Bond
ATTN: NMR

Defense Documentation Center
12 cy ATTN: TC

Director
Defense Intelligence Agency
ATTN: DI-7D, Edward O'Farrell

Director
Defense Nuclear Agency
ATTN: STSI, Archives
ATTN: RATN
ATTN: DDST
2 cy ATTN: STTL, Tech. Lib.
2 cy ATTN: RAEV

Commander
Field Command, DNA
ATTN: FCLMC
ATTN: FCPR

Director
Interservice Nuclear Weapons School
ATTN: Doc. Con.

Director
Joint Strategic Target Planning Staff, JCS
ATTN: JLTW-2

Chief
Livermore Division, Field Command, DNA
ATTN: Doc. Con. for L-395
ATTN: FCPRL

National Communications Systems
Office of the Manager
ATTN: NCS-TS, Charles D. Bodson

Director
National Security Agency
ATTN: Orland O. Van Gunten, R-425

DEPARTMENT OF DEFENSE (Continued)

OJCS/J-3
ATTN: J-3, RDTA Br., WWMCCS, Plans Div.

OJCS/J-5
ATTN: J-5, Plans & Policy, R & D Div.

Commander-in-Chief
U.S. European Command, JCS
ATTN: ECJ6-P

DEPARTMENT OF THE ARMY

Director
Ballistic Missile Defense Advanced Technical Center
ATTN: RDMH-O, F. M. Hoke

Commander
Ballistic Missile Defense System Command
ATTN: BDMSC-TEN, Noah J. Hurst
ATTN: SSC-TEN, L. L. Dickerson

Deputy Chief of Staff for Research Development & Acq.
ATTN: DAMA-CSM-N,
Lieutenant Colonel E. V. DeBoeser, Jr.

Commander
Harry Diamond Laboratories
ATTN: DRXDO-RCC, Raine Gilbert
ATTN: DRXDO-EM, R. Bostak
ATTN: DRXDO-RCC, John A. Rosado
ATTN: DRXDO-EM, George Merkel
ATTN: DRXDO-TI, Tech. Lib.
ATTN: DRXDO-RBH, Stewart S. Graybill
ATTN: DRXDO-RC, Robert B. Oswald, Jr.
ATTN: DRXDO-EM, John Bombardt
ATTN: DRXDO-RCC, John E. Thompkins
ATTN: DRXDO-RB, Joseph R. Miletta
ATTN: DRXDO-TR, Edward E. Conrad
ATTN: DRXDO-NP, Francis N. Wimenitz
ATTN: DRXDO-RB, Robert E. McCoskey

Commander
Picatinny Arsenal
ATTN: SARPA-ND-C-E, Amina Nordio
ATTN: SARPA-FR-E, Louis Avrami
ATTN: SMUPA-ND-W
ATTN: SMUPA-TN, Burton V. Franks
ATTN: SARPA-TS-I-E, Abraham Grinoch
ATTN: SARPA-ND-N-D

Commander
Redstone Scientific Information Center
4 cy ATTN: AMSMI-RBD, Clara T. Rogers

Commander
TRASANA
ATTN: ATAA-EAC, Francis N. Winans

Director
U.S. Army Ballistic Research Labs.
ATTN: DRXBR-AM, Donald Eccleshall

Chief
U.S. Army Communications Sys. Agency
ATTN: SCCM-AD-SV, Library

DEPARTMENT OF THE ARMY (Continued)

Commander
U.S. Army Electronics Command
ATTN: DRSEL-TL-ME, M. W. Pomerantz
ATTN: DRSEL-NL-O-4
ATTN: DRSEL-GG-TD, W. R. Werk
ATTN: DRSEL-TL-IR, Edwin T. Hunter
ATTN: DRSEL-PL-ENV, Hans A. Bomke

Division Engineer
U.S. Army Engr. Div., Missouri River
ATTN: MRDED-MC, Floyd L. Hazlett

Commander-in-Chief
U.S. Army Europe & Seventh Army
ATTN: ODCSE-E, AEAGE-PI

Commandant
U.S. Army Field Artillery School
ATTN: ATSFA-CTD-ME, Harley Moberg

Commander
U.S. Army Foreign Science & Tech. Ctr.
ATTN: DRXST-ISI, Daniel W. McCallum, Jr.

Commander
U.S. Army Mat. & Mechanics Research Ctr.
ATTN: DRXMR-HH, John F. Dignam

Commander
U.S. Army Materiel Dev. & Readiness Command
ATTN: DRCDE-D, Lawrence Flynn

Commander
U.S. Army Missile Command
ATTN: DRCPM-PE-EG, William .. Johnson

Commander
U.S. Army Safeguard Command
ATTN: Chief, Activation Division

Commander
U.S. Army Test & Evaluation Command
ATTN: DRSTE-EL, Richard I. Kolchin
ATTN: DRSTE-NB, Russell R. Galasso

DEPARTMENT OF THE NAVY

Chief of Naval Operations
ATTN: Code 604C3, Robert Piacesi
ATTN: Robert A. Blaise

Chief of Naval Research
ATTN: Code 464, Thomas P. Quinn
ATTN: Code 427, Henry Mullaney

Commander
Naval Air Systems Command
ATTN: AIR-5202, Muriel L. Scarbough

Commander
Naval Electronic Systems Command
ATTN: Code 5032, Charles W. Neill
ATTN: PME 117-T
ATTN: PME 117-21

Commander
Naval Electronics Laboratory Center
ATTN: Code 3100, E. E. McCown

DEPARTMENT OF THE NAVY (Continued)

Commanding Officer
Naval Intelligence Support Ctr.
ATTN: NISC-611

Director
Naval Research Laboratory
ATTN: Code 7770, Gerald Cooperstein
ATTN: Code 7701, Jack D. Brown
ATTN: Code 6631, James C. Ritter
ATTN: Code 7706, Jay P. Boris
ATTN: Code 2627, Doris R. Folen
ATTN: Code 4004, Emanual L. Brancato

Commander
Naval Sea Systems Command
ATTN: SEA-9931, Riley B. Lane
ATTN: SEA-9931, Samuel A. Barham

Commander
Naval Ship Engineering Center
ATTN: Code 6174D2, Edward F. Duffy

Commander
Naval Surface Weapons Center
ATTN: Code WA-50, John H. Malloy
ATTN: Code 431, Edwin B. Dean
ATTN: Code WX-21, Tech. Lib.
ATTN: Code 431, Edwin R. Rathburn
ATTN: Code WA-501, Navy Nuc. Prgms. Off.

Commander
Naval Telecommunications Command
ATTN: N-7, LCDR Hall

Commander
Naval Weapons Center
ATTN: Code 533, Tech. Lib.

Commanding Officer
Naval Weapons Evaluation Facility
ATTN: Lawrence R. Oliver

Commanding Officer
Naval Weapons Support Center
ATTN: Code 70242, Joseph A. Munarin
ATTN: Code 7024, James Ramsey

Director
Strategic Systems Project Office
ATTN: NSP-2431, Gerald W. Hoskins
ATTN: NSP-2701, John W. Pitsenberger
ATTN: NSP-230, David Gold

DEPARTMENT OF THE AIR FORCE

Commander
ADC/DE
ATTN: DEEDS, Joseph C. Brannan

Commander
Aeronautical Systems Division, AFSC
ATTN: 4950 Test, W/TZMH, Peter T. Marth
ATTN: ASD-YH-EX, Lt Col Robert Leverette

AF Geophysics Laboratory, AFSC
ATTN: Charles Pike
ATTN: LQR, Edward A. Burke

DEPARTMENT OF THE AIR FORCE (Continued)

AF Institute of Technology, AU
ATTN: Library, AFIT, Bldg. 640, Area B

AF Materials Laboratory, AFSC
ATTN: Library

AF Weapons Laboratory, AFSC
ATTN: SAS
ATTN: SAB
ATTN: EL, John Darrah
ATTN: ELA
ATTN: ELC
ATTN: SUL
ATTN: EL

Headquarters
Electronic Systems Division, AFSC
ATTN: DCD/SATIN IV
ATTN: XRRT

Commander
Foreign Technology Division, AFSC
ATTN: ETET, Capt Richard C. Husemann

HQ USAF/RD
ATTN: RDQPN

SAMSO/DY
ATTN: DYS, Capt Wayne Schober
ATTN: DYS, Maj Larry A. Darda

SAMSO/IN
ATTN: IND, Maj Darryl S. Muskin

SAMSO/MN
ATTN: MNNH, Capt Michael V. Bell
ATTN: MNNG, Capt David J. Strobel
ATTN: MNNG
ATTN: MNNH, Capt William M. Carra

SAMSO/SK
ATTN: SKF, Peter H. Stadler

SAMSO/XR
ATTN: XRS

SAMSO/YD
ATTN: YDD, Maj Marion F. Schneider

Commander in Chief
Strategic Air Command
ATTN: NRI-STINFO Library
ATTN: XPFS, Capt Deraad

ENERGY RESEARCH & DEVELOPMENT ADMINISTRATION

University of California
Lawrence Livermore Laboratory
ATTN: Walter W. Hofer, L-24
ATTN: Donald J. Meeker, L-545
ATTN: Louis F. Wouters, L-48
ATTN: Tech. Info., Dept. L-3
ATTN: William J. Hogan, L-531
ATTN: Frederick R. Kovar, L-31
ATTN: Hans Kruger, L-96
ATTN: Donald W. Vollmer, L-154

ENERGY RESEARCH & DEVELOPMENT ADMINISTRATION (Continued)

Los Alamos Scientific Laboratory
ATTN: Doc. Con. for P. W. Keaton
ATTN: Doc. Con. for Donald R. Westervelt
ATTN: Doc. Con. for Bruce W. Noel
ATTN: Doc. Con. for Reports Lib.
ATTN: Doc. Con. for J. Arthur Freed
ATTN: Doc. Con. for John S. Malik
ATTN: Doc. Con. for Marvin M. Hoffman
ATTN: Doc. Con. for Richard L. Wakefield

Sandia Laboratories
Livermore Laboratory
ATTN: Doc. Con. for Theodore A. Dellin

Sandia Laboratories
ATTN: Doc. Con. for 3141, Sandia Rpt. Coll.
ATTN: Doc. Con. for Org. 2315, James E. Gover
ATTN: Doc. Con. for Org. 2110, J. A. Hood
ATTN: Doc. Con. for Elmer F. Hartman
ATTN: Doc. Con. for 5240, Gerald Yonas
ATTN: Doc. Con. for Org. 9353, R. L. Parker
ATTN: Div. 5231, James H. Renken

OTHER GOVERNMENT AGENCIES

Administrator
Defense Electric Power Admin.
ATTN: Doc. Con.

Department of Commerce
National Bureau of Standards
ATTN: Judson C. French

Department of Transportation
Federal Aviation Administration
ATTN: Fredrick S. Sakate, ARD-350

NASA
ATTN: Code Res. Guid. Con. & Info. Sys.

NASA
ATTN: Robert R. Lovell, M.S. 54-3
ATTN: Library

DEPARTMENT OF DEFENSE CONTRACTORS

Aerojet Electro-Systems Co. Div.
Aerojet-General Corporation
ATTN: Thomas D. Hanscome

Aeronutronic Ford Corporation
ATTN: Library
ATTN: J. T. Mattingley, M.S. X-22
ATTN: Donald R. McMorrow, M.S. G-30

Aerospace Corporation
ATTN: Library
ATTN: Norman D. Stockwell
ATTN: V. Josephson
ATTN: William W. Willis
ATTN: Frank Hai
ATTN: Irving M. Garfunkel
ATTN: C. B. Pearlston
ATTN: Julian Reinheimer
ATTN: J. Benveniste

Avco Research & Systems Group
ATTN: Research Library, A-830, Rm. 7201

DEPARTMENT OF DEFENSE CONTRACTORS (Continued)

Battelle Memorial Institute
ATTN: Robert H. Blazek

The BDM Corporation
ATTN: T. H. Neighbors

The Bendix Corporation
Navigation & Control Division
ATTN: George Gartner

The Boeing Company
ATTN: Aerospace Library
ATTN: Kenneth D. Friddell, M.S. 2R-00
ATTN: David L. Dye, M.S. 87-75
ATTN: Donald W. Egelkrout, M.S. 2R-00
ATTN: Howard W. Wicklein, M.S. 17-11
ATTN: Robert S. Caldwell, 2R-00

Booz-Allen & Hamilton, Inc.
ATTN: Raymond J. Chrisner

Brown Engineering Company, Inc.
ATTN: John M. McSwain, M.S. 18

Burroughs Corporation
ATTN: Robert L. Davis, Rm. G-321

University of California at San Diego
ATTN: Sherman De Forest

Charles Stark Draper Laboratory, Inc.
ATTN: Richard G. Haltmaier
ATTN: Kenneth Fertig
ATTN: Paul R. Kelly

Computer Sciences Corporation
ATTN: Barbara F. Adams

Computer Sciences Corporation
ATTN: Richard H. Dickhaut
ATTN: Alvin T. Schiff

Cutler-Hammer, Inc.
ATTN: Central Tech. Files, Anne Anthony

Dr. Eugene P. dePlomb
ATTN: Eugene P. dePlomb

The Dikewood Corporation
ATTN: K. Lee
ATTN: Tech. Lib.

E-Systems, Inc.
ATTN: Library, 8-50100

EG&G, Inc.
Albuquerque Division
ATTN: Tech. Lib.
ATTN: Hilda H. Hoffman

Exp. & Math Physics Consultants
ATTN: Thomas M. Jordan

Fairchild Camera & Instrument Corp.
ATTN: Sec. Dept. for 2-233, David K. Myers

The Franklin Institute
ATTN: Ramie H. Thompson

DEPARTMENT OF DEFENSE CONTRACTORS (Continued)

General Electric Company
Space Division
ATTN: John L. Andrews
ATTN: John R. Greenbaum
ATTN: James P. Spratt
ATTN: Joseph C. Peden, VFSC, Rm. 4230M
ATTN: Larry I. Chasen
ATTN: Daniel Edelman

General Electric Company
Re-Entry & Environmental Systems Div.
ATTN: Robert V. Benedict

General Electric Company
TEMPO-Center for Advanced Studies
ATTN: Royden R. Rutherford
ATTN: William McNamara
ATTN: John D. Illgen
ATTN: DASIAC

General Electric Company
ATTN: CSP 6-7, Richard C. Fries

General Electric Company
Aircraft Engine Group
ATTN: John A. Ellerhorst, E-2

General Electric Company
Aerospace Electronics Systems
ATTN: W. J. Patterson, Drop 233
ATTN: Charles M. Hewison, Drop 624

General Research Corporation
ATTN: John Ise, Jr.

General Research Corporation
Washington Operations
ATTN: David K. Osias

Goodyear Aerospace Corporation
Arizona Division
ATTN: B. Manning

Grumman Aerospace Corporation
ATTN: Jerry Rogers, Dept. 533

GTE Sylvania, Inc.
Electronics Systems Grp.-Eastern Div.
ATTN: Charles A. Thornhill, Librarian
ATTN: Leonard L. Blaisdell

GTE Sylvania, Inc.
ATTN: David P. Flood
ATTN: Herbert A. Ullman
ATTN: H & V Group, Mario A. Nurefora
ATTN: Comm. Sys. Div., Emil P. Motchok
ATTN: A.S.M. Dept., S. E. Perlman

Hazeltine Corporation
ATTN: Tech. Info. Ctr., M. Waite

Hercules, Incorporated
ATTN: W. R. Woodruff, 100K-26

Honeywell, Incorporated
Government & Aeronautical Products Division
ATTN: Ronald R. Johnson, A-1622

DEPARTMENT OF DEFENSE CONTRACTORS (Continued)

Honeywell, Incorporated
Aerospace Division
ATTN: Harrison H. Noble, M.S. 725-5A
ATTN: Richard B. Reinecke, M.S. 725-5

Honeywell, Incorporated
ATTN: Tech. Lib.

Hughes Aircraft Company
ATTN: Tech. Lib.
ATTN: Kenneth R. Walker, M.S. D-157
ATTN: Billy W. Campbell, M.S. 6-E-110
ATTN: John B. Singletary, M.S. 6-D-133

Hughes Aircraft Company
Space Systems Division
ATTN: Edward C. Smith, M.S. A-620
ATTN: William W. Scott, M.S. A-1080

IBM Corporation
ATTN: Frank Frankovsky

IIT Research Institute
ATTN: Irving N. Mindel
ATTN: Jack E. Bridges

Institute for Defense Analyses
ATTN: IDA, Librarian, Ruth S. Smith

Intelcom Rad Tech
ATTN: Dennis Swift
ATTN: Terry Flanagan
ATTN: R. L. Mertz
ATTN: James A. Naber

International Telephone & Telegraph Corporation
ATTN: Alexander T. Richardson

Ion Physics Corporation
ATTN: Robert D. Evans

Jaycor, Incorporated
ATTN: Andrew Woods
ATTN: Eric P. Wenaas

Johns Hopkins University
Applied Physics Laboratory
ATTN: Peter E. Partridge

Kaman Sciences Corporation
ATTN: Donald H. Bryce
ATTN: John R. Hoffman
ATTN: Library
ATTN: W. Foster Rich
ATTN: R. J. Fisher
ATTN: R. L. Hartman
ATTN: Walter E. Ware
ATTN: Albert P. Bridges

Litton Systems, Inc.
Guidance & Control Systems Division
ATTN: R. W. Maughmer
ATTN: John P. Retzler
ATTN: Val J. Ashby, M.S. 67

Lockheed Missiles & Space Company
ATTN: Clarence F. Kooi, Dept. 52-11

DEPARTMENT OF DEFENSE CONTRACTORS (Continued)

Lockheed Missiles & Space Co., Inc.
ATTN: Samuel I. Taimuty, Dept. 85-85
ATTN: George E. Heath, Dept. 81-14
ATTN: Philip J. Hart, Dept. 81-14
ATTN: Edwin A. Smith, Dept. 85-85
ATTN: Benjamin T. Kimura, Dept. 81-14

LTV Aerospace Corporation
Vought Systems Division
ATTN: Charles H. Coleman

LTV Aerospace Corporation
Michigan Division
ATTN: Tech. Lib.
ATTN: James F. Sanson, B-2

M.I.T. Lincoln Laboratory
ATTN: Jean L. Ryan
ATTN: Leona Loughlin, Librarian, A-082

Martin Marietta Aerospace
Orlando Division
ATTN: William W. Mras, MP-413
ATTN: Mona C. Griffith, Lib., MP-30
ATTN: Jack M. Ashford, MP-537

Martin Marietta Corporation
Denver Division
ATTN: Ben T. Graham, M.S. PO-454
ATTN: J. E. Goodwin, Mail 0452

Maxwell Laboratories, Inc.
ATTN: Victor Fargo

McDonnell Douglas Corporation
ATTN: Chester G. Polak

McDonnell Douglas Corporation
ATTN: Stanley Schneider
ATTN: Paul H. Duncan, Jr.

Mission Research Corporation
ATTN: Daniel F. Higgins
ATTN: Roger Stettner
ATTN: Conrad L. Longmire
ATTN: William C. Hart

Mission Research Corporation
ATTN: David E. Merewether
ATTN: Larry D. Scott

Mission Research Corporation, San Diego
ATTN: V. A. J. Van Lint

The Mitre Corporation
ATTN: Theodore Jarvis

Motorola, Inc.
Government Electronics Division
ATTN: James R. Black, M.S. A-112
ATTN: A. J. Kordalewski, Tech. Info. Ctr.

Northrop Corporation
Electronic Division
ATTN: John M. Reynolds
ATTN: Vincent R. DeMartino
ATTN: Boyce T. Ahlport

DEPARTMENT OF DEFENSE CONTRACTORS (Continued)

Northrop Corporation
ATTN: Orlie L. Curtis, Jr.
ATTN: David N. Pocock
ATTN: Library

Northrop Corporation
Electronic Division
ATTN: Joseph D. Russo

Physics International Company
ATTN: Doc. Con. for John H. Huntington
ATTN: Doc. Con. for Philip W. Spence
ATTN: Doc. Con. for Ian D. Smith
ATTN: Doc. Con. for Charles H. Stallings

Pulsar Associates, Inc.
ATTN: Carleton H. Jones, Jr.

R & D Associates
ATTN: Leonard Schlessinger
ATTN: S. Clay Rogers
ATTN: William R. Graham, Jr.
ATTN: Richard R. Schaefer
ATTN: William J. Karzas

The Rand Corporation
ATTN: Cullen Crain

Raytheon Company
ATTN: Gajanan H. Joshi, Radar Sys. Lab.

Raytheon Company
ATTN: Harold L. Flescher
ATTN: Jame. R. Weckback

RCA Corporation
Government & Commercial Systems
ATTN: George J. Brucker

RCA Corporation
ATTN: K. H. Zaininger

RCA Corporation
Government & Commercial Systems
ATTN: Eleanor K. Daly
ATTN: Andrew L. Warren

RCA Corporation
ATTN: E. Van Keuren, 13-5-2

Research Triangle Institute
ATTN: Sec. Officer for Eng. Div., Mayrant Simons, Jr.

Rockwell International Corporation
ATTN: Donald J. Stevens, FA-70
ATTN: L. H. Pinson, FB-41
ATTN: N. J. Rudie, FA-53
ATTN: J. Spetz
ATTN: George C. Messenger, FB-61
ATTN: James E. Bell, HA-10

Texas Instruments, Inc.
ATTN: Donald J. Manus, M.S. 72

Texas Tech University
ATTN: Travis L. Simpson

DEPARTMENT OF DEFENSE CONTRACTORS (Continued)

Rockwell International Corporation
ATTN: John F. Roberts

Rockwell International Corporation
ATTN: T. B. Yates

Sanders Associates, Inc.
ATTN: James L. Burrows
ATTN: Moe L. Aitel, NCA 1-3236
ATTN: R. G. Despathy, Sr., P E, 1-6270

Science Applications, Inc.
ATTN: William L. Chadsey

Science Applications, Inc.
Huntsville Division
ATTN: Noel R. Byrn

Science Applications, Inc.
ATTN: J. Roger Hill

Science Applications, Inc.
ATTN: Charles Stevens

Sidney Frankel & Associates
ATTN: Sidney Frankel

Simulation Physics, Inc.
ATTN: Roger G. Little

The Singer Company
ATTN: Irwin Goldman, Eng. Management

Sperry Flight Systems Division
Sperry Rand Corporation
ATTN: D. Andrew Schow

Sperry Rand Corporation
Univac Division
ATTN: James A. Inda, M.S. 41T25

Sperry Rand Corporation
Sperry Division
ATTN: Paul Marraffino
ATTN: Charles L. Craig, EV

Stanford Research Institute
ATTN: Robert A. Armistead
ATTN: Setsuo Dairiki
ATTN: Mel Bernstein
ATTN: Philip J. Dolan
ATTN: Arthur Lee Whitson

Stanford Research Institute
ATTN: MacPherson Morgan

Sundstrand Corporation
ATTN: Curtis B. White

Systems, Science & Software
ATTN: David A. Meskan

Systems, Science & Software, Inc.
ATTN: Ira Katz
ATTN: Andrew R. Wilson

Systron-Donner Corporation
ATTN: Harold D. Morris

DEPARTMENT OF DEFENSE CONTRACTORS (Continued)

TRW Systems Group
ATTN: Robert M. Webb, M.S. R1-1150
ATTN: Tech. Info. Ctr., S-1930
ATTN: William H. Robinette, Jr.
ATTN: Jerry I. Lubell
ATTN: Aaron H. Narevsky, R1-2144
ATTN: Lillian D. Singletary, R1-1070
ATTN: Philip R. Garder, R1-1028
ATTN: Richard H. Kingsland, R1-2154
ATTN: Donald Jortner
ATTN: Paul Molmud, R1-1196

TRW Systems Group
San Bernardino Operations
ATTN: J. M. Gorman
ATTN: Earl W. Allen
ATTN: John E. Dahnke

DEPARTMENT OF DEFENSE CONTRACTORS (Continued)

TRW Systems Group
ATTN: Donald W. Pugsley

United Technologies Corporation
Norden Division
ATTN: Conrad Corda

Westinghouse Electric Corporation
ATTN: Henry P. Kalapaca, M.S. 3525